

# Disk Evolution Study Through Imaging of Nearby Young Stars (DESTINYs): PDS 111, an old T Tauri star with a young-looking disk

Annelotte Derkink<sup>1</sup>, Christian Ginski<sup>2</sup>, Paola Pinilla<sup>3</sup>, Nicolas Kurtovic<sup>4</sup>, Lex Kaper<sup>1</sup>, Alex de Koter<sup>1,5</sup>, Per-Gunnar Valegård<sup>1</sup>, Eric Mamajek<sup>6,7</sup>, Frank Backs<sup>1</sup>, Myriam Benisty<sup>8,9</sup>, Til Birnstiel<sup>10</sup>, Gabriele Columba<sup>11</sup>, Carsten Dominik<sup>1</sup>, Antonio Garufi<sup>12</sup>, Michiel Hogerheijde<sup>1,13</sup>, Rob van Holstein<sup>14</sup>, Jane Huang<sup>15</sup>, François Ménard<sup>9</sup>, Christian Rab<sup>10,4</sup>, María Claudia Ramírez-Tannus<sup>16</sup>, Álvaro Ribas<sup>17</sup>, Jonathan P. Williams<sup>18</sup>, and Alice Zurlo<sup>19,20</sup>

(Affiliations can be found after the references)

## ABSTRACT

**Context.** The interplay between T Tauri stars and their circumstellar disks, and how this impacts the onset of planet formation has yet to be established. In the last years, major progress has been made using instrumentation that probes the dust structure in the mid-plane and at the surface of protoplanetary disks. Observations show a great variety of disk shapes and substructures that are crucial for understanding planet formation.

**Aims.** We studied a seemingly old T Tauri star, PDS 111, and its disk. We combined complementary observations of the stellar atmosphere, the circumstellar hot gas, the surface of the disk, and the mid-plane structure.

**Methods.** We analyzed optical, infrared, and sub-millimeter observations obtained with VLT/X-shooter, Mercator/HERMES, TESS, VLT/SPHERE, and ALMA, providing a new view on PDS 111 and its protoplanetary disk. The multi-epoch spectroscopy yields photospheric lines to classify the star and to update its stellar parameters, and emission lines to study variability in the hot inner disk and to determine the mass-accretion rate. The SPHERE and ALMA observations are used to characterize the dust distribution of the small and large grains, respectively.

**Results.** PDS 111 is a weak-line T Tauri star with spectral type G2, exhibits strong H $\alpha$  variability and with a low mass-accretion rate of  $1 - 5 \times 10^{-10} M_{\odot} \text{ yr}^{-1}$ . We measured an age of the system of  $15.9_{-3.7}^{+1.7}$  Myr using pre-main sequence tracks. The SPHERE observations show a strongly flaring disk with an asymmetric substructure. The ALMA observations reveal a 30 au cavity in the dust continuum emission with a low contrast asymmetry in the South-West of the disk and a dust disk mass of  $45.8 M_{\oplus}$  or  $\sim 0.14 M_{\text{Jup}}$ . The  $^{12}\text{CO}$  observations do not show a cavity and the  $^{12}\text{CO}$  radial extension is at least three times larger than that of the dust emission.

**Conclusions.** Although the measured age is younger than often suggested in literature, PDS 111 seems relatively old; this provides insight into disk properties at an advanced stage of pre-main sequence evolution. The characteristics of this disk are very similar to its younger counterparts: strongly flaring, an average disk mass, a typical radial extent of the disk gas and dust, and the presence of common substructures. This suggests that disk evolution has not significantly changed the disk properties. These results show similarities with the "Peter Pan disks" around M-dwarfs, that "refuse to evolve".

**Key words.** protoplanetary disks, star: PDS 111, stars: pre-main sequence

## 1. Introduction

Disk evolution seems inherently connected to the formation of planets in circumstellar disks around low-mass pre-main-sequence (PMS) stars. Some of the big questions are when, where, and how planets, in all their observed varieties, exactly form. A thorough understanding of disk evolution is key to understand the onset of planet formation in these environments.

An important aspect of the evolution of a disk is how matter is distributed, for instance how dust grains with different sizes are distributed vertically, radially and within substructures. In recent years, major progress has been made using telescopes and instruments that are able to probe the mid-plane structure and surface of the disk (e.g., ALMA and VLT/SPHERE). Extensive observations show great variety in disk shapes (e.g., Avenhaus et al. 2018; Law et al. 2023) and substructures in the form of cavities, rings, spiral arms, and arcs (e.g., Long et al. 2018; Andrews et al. 2018; Garufi et al. 2020; Andrews 2020; Benisty et al. 2023; Bae et al. 2023).

These substructures are thought to trace active sites in the disk, where planetesimals may grow and act as an indication of planet formation (Andrews 2020). This makes the study of these substructures important to uncover disk evolution and disk-planet interactions. For example, Pinilla et al. (2018) studied

transition disks with cavities and identified giant planet formation and dead zones as potential explanations for the observed properties of these disks. Another large study of disk substructures from Garufi et al. (2020) with ALMA and SPHERE shows that rings and cavities detected with ALMA do not always have a similar SPHERE counterpart, demonstrating the importance of combined and complementary observations.

Disks around PMS stars have limited time to form planets since they are thought to dissipate rapidly. Large surveys of T Tauri stars have shown that only a few percent of the disks survive beyond an age of 10 Myr (Padgett et al. 2006; Carpenter et al. 2009; Wahhaj et al. 2010). However, recently so-called "Peter Pan Disks" have been discovered around M-type stars. These systems have accretion disks older than 20 Myr that "refuse to grow up". These disks are thought to be long-lived due to a high initial disk mass with a low turbulence parameter and a lack of external photo-evaporation (Sicilia-Aguilar et al. 2011; Silverberg et al. 2020; Coleman & Haworth 2020).

In this paper, we combine SPHERE and ALMA observations with medium-resolution spectroscopy of the star and the hot inner disk in order to infer a detailed picture of the system PDS 111. This T Tauri star, often classified as G-type (Rojas et al. 2008), is known to be in the foreground of the Orion

star-forming region at a distance of 158 pc (Gaia Collaboration 2022) with a relatively high age (15–42 Myr, Rojas et al. 2008; Bell et al. 2015; Launhardt et al. 2022). However, this system seems to be one of these rare cases where the circumstellar disk has survived up until this significant age. The aim of this work is to reassess the age determination of the system and to measure its disk properties in order to understand how PDS 111 fits in the current understanding of disk evolution, and how this relates to the long-lived disks in the "Peter Pan Disk" scenario.

In the following, we describe the observations in Sec. 2 and the data analysis of the photospheric light, scattered light, dust continuum and  $^{12}\text{CO}$  emission in Sec. 3. The age of the system and the disk properties are presented in Sec. 4. We discuss the results in Sec. 5 and summarize our findings in Sec. 6.

## 2. Observations

PDS 111 was observed in the framework of the Disk Evolution Study Through Imaging of Nearby Stars (DESTINYs) ESO large program (Ginski et al. 2020, 2021). Resolved high-resolution imaging observations were carried out with the extreme adaptive optics instrument VLT/SPHERE (Beuzit et al. 2019). Additionally, we obtained sub-mm observations with ALMA, medium-resolution spectroscopic observations of the central star with VLT/X-shooter (Vernet et al. 2011), high-resolution spectroscopy with Mercator/HERMES (Raskin et al. 2011) and we used photometric observations from the Transiting Exoplanet Survey Satellite mission (TESS Ricker et al. 2015).

### 2.1. Spectroscopy

#### 2.1.1. X-shooter medium resolution spectroscopy

Spectroscopic observations in the optical to near infrared (NIR) (300–2500 nm) have been taken with X-shooter, mounted on the UT2 of the VLT, with program ID 108.2216.001. PDS 111 was observed with X-shooter during two separate epochs on November 28, 2021 and December 7, 2021. The first observation has been taken with a poor seeing of  $\sim 2.6''$  and the second under good seeing conditions of  $\sim 0.7''$ . Both observations can be used in the study. The spectra are taken in nodding mode. The used slit widths are  $0.5''$  in the UVB arm leading to a resolving power of 9700, and  $0.4''$  in the VIS and NIR arms, which corresponds to a resolving power of 18400 and 11600, respectively.

The spectroscopic data were reduced with the ESO X-shooter pipeline 3.3.5 provided by ESO (Modigliani et al. 2010). The pipeline consists of a flat-field correction, bias subtraction, and wavelength calibration. Spectrophotometric standards from the ESO database were used for flux calibration. The reduction of the nodding spectra was done with the `xsh_scired_slit_nod` recipe provided in the software package from ESO. The `Molecfit` 1.5.9 tool was used to correct for the telluric sky lines in the spectra (Smette et al. 2015; Kausch et al. 2015).

The arms are normalized separately using second-order spline functions. The continuum points for the spline fit are selected at the same wavelength intervals for each epoch.

#### 2.1.2. HERMES high resolution spectroscopy

High-resolution follow-up observations have been taken with the HERMES spectrograph (380–900 nm) mounted on the *Mercator* 1.2 m telescope on La Palma (Raskin et al. 2011) to obtain a longer temporal baseline for line variability. HERMES has a

spectral resolving power of  $R \sim 85,000$ . Observations were taken on two nights, October 20, 2022 and October 28, 2022. The data were reduced with the standard HERMES pipeline, consisting of a flat-field correction, bias subtraction, wavelength calibration, and cosmic removal. The humidity was relatively high ( $\sim 50\%$ ) for the second observation compared to the first observation, introducing stronger telluric features. The spectra were rebinned on the same resolution as X-shooter to increase the signal-to-noise ratio and similarly normalized in order to compare the spectra of HERMES and X-shooter.

### 2.2. SPHERE/IRDIS near-infrared imaging

PDS 111 was observed with the InfraRed Dual-band Imager and Spectrograph (IRDIS, Dohlen et al. 2008) subsystem of SPHERE on December 30, 2020. The observations were carried out in the BB\_H filter with a central wavelength of  $1.65 \mu\text{m}$ . We used the dual-beam polarimetric imaging mode of the instrument (de Boer et al. 2020; van Holstein et al. 2020) in pupil-tracking mode (van Holstein et al. 2017). The central star was placed behind an apodized Lyot coronagraph with an effective radius of  $92.5 \text{ mas}$  to avoid saturation and to limit photon noise. We recorded a total of 104 science frames split into 26 polarimetric cycles. The individual frame exposure time was 32 s resulting in a total exposure time of 55.5 min. The atmospheric conditions during the observation sequence were excellent with an average seeing of  $0.72''$  and a coherence time of 9.8 ms. Bracketing the science observations we acquired dedicated astrometric star-center and flux calibration frames, as well as sky calibration frames.

We reduced the data using the IRDIS Data reduction for Accurate Polarimetry<sup>1</sup> pipeline (IRDAP, van Holstein et al. 2020), which performs polarimetric differential imaging (PDI, Kuhn et al. 2001) to remove the light from the bright central star. We used the default setup parameters. IRDAP first performs image pre-processing, which includes sky subtraction, flat-fielding, and bad-pixel masking. A static master flat-field image, as well as a static badpixel mask were used, which are included in IRDAP. Then the frames were separated in the left and right detector side and individually centered, using the astrometric star-center calibration frames. After these pre-processing steps IRDAP combines images from both detector sides, as well as images at different half-wave plate position to compute the Stokes  $Q$  and  $U$  images. To remove residual instrumental polarization a full Mueller matrix model of the telescope and instrument is implemented that describes the instrumental polarization effects. Additionally, residual (inter)stellar polarization is removed by measuring the signal at the adaptive optics correction radius within the  $Q$  and  $U$  images and subtracting a scaled total intensity image. The final  $Q$  and  $U$  images are then converted into the azimuthal Stokes parameters  $Q_\phi$  and  $U_\phi$ , following the definition in de Boer et al. (2020). The  $Q_\phi$  image contains all azimuthally polarized light as positive signal. Since this is the expected orientation of the polarization direction for single scattering events it gives a good representation of the disk polarized light image. We show the  $Q_\phi$  image in Fig. 1 and the full set of Stokes images in the Appendix (Fig. A.1).

In addition to the PDI reduction, we performed angular differential imaging (ADI, Marois et al. 2006) post-processing with the IRDAP pipeline. We used the principal component analysis approach to fit the reference catalog (consisting of all science images themselves) to each science frame. For the processing

<sup>1</sup> <https://irdap.readthedocs.io>

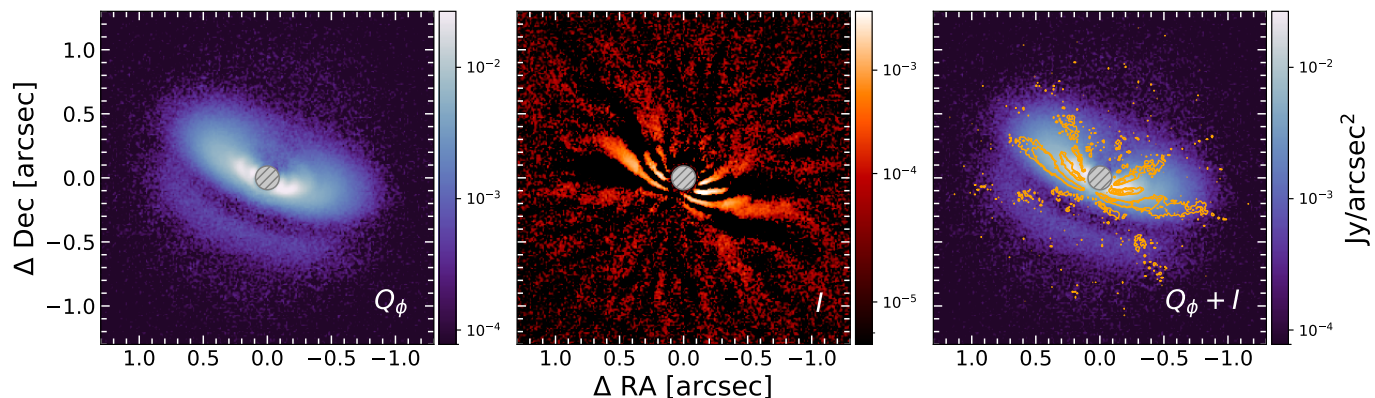


**Fig. 1.** SPHERE/IRDIS H-band ( $1.65 \mu\text{m}$ ) observations of PDS 111. In all images the star is at the center and the images are aligned with the North-axis up and East-axis to the left. *Left:* Polarized light observation. We show the azimuthal Stokes parameter  $Q_\phi$  which contains all azimuthally polarized scattered light as a positive signal. *Middle:* Same data set as in the left panel, but reduced with angular differential imaging, showing total intensity. Due to the reduction approach, the disk signal is strongly self-subtracted removing particularly low spatial frequencies. The shape of the detected high spatial frequency sub-structure is likely distorted. For the same reason, the given surface brightness is a lower limit only, which depends in a complex way on the local self subtraction in the image. *Right:* Same image as in the left panel, overlaid with contours ( $5\sigma$ ,  $14\sigma$ ,  $68\sigma$ ,  $140\sigma$ ,  $205\sigma$ ; relative to the image background noise) from the center panel to highlight the structures that are traced in both images. In all images, the gray, hashed circle in the center marks the area that was covered by the coronagraphic mask and where the star is located. All images are shown on a log scale to highlight the disk morphology. Appendix A shows a flux calibrated version of the polarimetric image.

the default settings of IRDAP were utilized. The ADI processed total intensity image is likewise shown in Fig. 1. For this image we specifically used 4 principal components and optimization annuli between 10 and 30 pixels ( $0.12''$  to  $0.37''$ ), 30 and 100 pixels ( $0.37''$  to  $1.23''$ ), and 100 and 512 pixels ( $1.23''$  to  $6.27''$ ).

### 2.3. ALMA observations

The  $1.25 \text{ mm}$  emission of PDS 111 was observed with ALMA Band 6 as part of the ALMA project 2021.1.01705.S (PI: C. Ginski), with 1.31 min of exposure on August 28, 2022 and 1.31 min in September 2, 2022. The correlator was configured to observe four spectral windows: one included the  $^{12}\text{CO}$  molecular line at  $230.538 \text{ GHz}$  in the  $J=2-1$  transition with a frequency spacing of  $488.3 \text{ kHz}$  ( $\sim 0.65 \text{ km s}^{-1}$  per channel), while the remaining three were targeted at dust continuum emission centered at  $233.519 \text{ GHz}$ ,  $246.020 \text{ GHz}$ , and  $248.021 \text{ GHz}$ , with a channel frequency spacing of  $15.625 \text{ MHz}$  and a total bandwidth of  $2 \text{ GHz}$ . The antenna baselines span  $15.1 \text{ m}$  to  $1210.6 \text{ m}$ .

Executing the `scriptforPI` provided by ALMA, we obtain the pipeline calibrated data, which is self-calibrated using dust continuum emission observations, so that the signal-to-noise ratio can be improved. Using CASA 5.6.2 we flagged the channels located at  $\pm 20 \text{ km s}^{-1}$  from the line center to obtain the dust continuum emission. A pseudo-continuum measurement set is created by combining the remaining channels with the continuum spectral windows. To reduce data volume, the set was averaged into  $125 \text{ MHz}$  channels and ‘6s’ bins. The self-calibration was applied on the continuum by imaging with the CLEAN algorithm, with a Briggs robust parameter of 0.5. The robust parameter is used to control the trade-off between the sensitivity and angular resolution of the data by applying a natural and/or uniform weighting scheme to the data. The value of 0.5 slightly favors angular resolution over sensitivity (Briggs 1995; Boone 2013). We applied four phase calibrations, using solution intervals of length ‘inf’, ‘40s’, ‘18s’, and ‘6s’, while the amplitude calibration was done with a solution interval of ‘6s’, combining

spectral windows and scans to find the solution. The correction tables were later applied to the  $^{12}\text{CO}$  spectral window.

After self-calibration, the continuum emission was imaged with a robust parameter of -0.5 to maximize the balance between angular resolution and sensitivity. The beam size of the  $^{12}\text{CO}$  is  $0.429''$ . The gas emission was imaged with a robust parameter of 0.0 and no visibility tapering to focus on best possible angular resolution. Both images were cleaned until the  $4\sigma$  noise level to apply the JvM correction (JvM ‘effect’ from Jorsater & van Moorsel 1995), which takes in account the volume ratio ( $\epsilon$ ) values of the point spread function of the images and the restored Gaussian from the CLEAN algorithm following the method as described in Czekala et al. (2021). We found  $\epsilon$  values of 0.909 for the dust continuum image and 0.694 for the  $^{12}\text{CO}$ , which means that the dirty beam shape for the dust continuum is more closely described by an elliptical Gaussian, while that for the  $^{12}\text{CO}$  imaging deviates more significantly.

### 2.4. TESS photometry

TESS observed PDS 111 during its runs starting in November and December 2018 (target name 24697724). The target was observed with exposures of 120 s during 42 days (spread between November, December, and January) with the TESS detector bandpass that spans from  $600 - 1000 \text{ nm}$ .

## 3. Data analysis

### 3.1. Photospheric spectrum PDS 111

Based on the strength of the G-band, Fe I lines and H $\gamma$  around  $432 \text{ nm}$ , the star is classified as early G-type (Gray 2000). A comparison of the spectrum with stars in the X-shooter library indicates a spectral class between G1 and G4. The luminosity class V is based on the relative strength of Mn I  $403.0 \text{ nm}$  and Fe I  $404.6 \text{ nm}$  and on the ratio between Ti II, Fe II  $417.2-8 \text{ nm}$ , and Ti II, Fe II  $444.4 \text{ nm}$  (see Fig. 2).

**Table 1.** Stellar parameters of PDS 111.

| Star parameter     | Value                    | unit                 | ref |
|--------------------|--------------------------|----------------------|-----|
| RA                 | 05 24 37.25              | h m s                | 1   |
| Dec                | -08 42 01.71             | ° ' ''               | 1   |
| $\mu_{RA}$         | $8.353 \pm 0.033$        | mas yr <sup>-1</sup> | 1   |
| $\mu_{Dec}$        | $-12.394 \pm 0.028$      | mas yr <sup>-1</sup> | 1   |
| Parallax           | $6.3136 \pm 0.0352$      | mas                  | 1   |
| Distance           | $157.85^{+0.95}_{-0.74}$ | pc                   | 4   |
| $v_{rad}$          | $25.8 \pm 0.1$           | km s <sup>-1</sup>   | 3   |
| Spectral Type      | G2 V                     |                      | 3   |
| $T_{eff}$          | $5900^{+100}_{-150}$     | K                    | 3   |
| log $g$ (spectrum) | $4.2 \pm 0.2$            | cm s <sup>-1</sup>   | 3   |
| log $g$ (SED)      | 4.13                     | cm s <sup>-1</sup>   | 3   |
| $G$                | 9.693                    | mag                  | 1   |
| $V$                | $9.97 \pm 0.22$          | mag                  | 2   |
| $B-V$              | $0.729 \pm 0.038$        | mag                  | 1   |
| Luminosity         | $2.52^{+0.75}_{-0.40}$   | $L_{\odot}$          | 3   |
| Radius             | $1.52^{+0.30}_{-0.17}$   | $R_{\odot}$          | 3   |
| $E(B-V)$           | 0.065                    | mag                  | 3   |
| $A_V$              | $0.2^{+0.2}_{-0.1}$      | mag                  | 3   |
| $P_{rot}$          | 3.1                      | days                 | 3   |
| Evolutionary mass  | $1.2^{+0.1}_{-0.1}$      | $M_{\odot}$          | 3   |
| Spectroscopic mass | 1.15 – 1.34              | $M_{\odot}$          | 3   |
| Age                | $15.9^{+1.7}_{-3.7}$     | Myr                  | 3   |
| inclination        | 58.2                     | °                    | 3   |
| $v \sin i$         | $21^{+0.4}_{-0.2}$       | km s <sup>-1</sup>   | 3   |

**References.** 1. Gaia Collaboration (2022) (ICRS, epoch 2000.0 calculated by VizieR), 2. Jayasinghe et al. (2018), 3. This work, 4. Bailer-Jones et al. (2021).

The temperature, surface gravity, and rotational velocity were constrained through the fitting of Kurucz models (Kurucz 1993) in the spectral range of 402–430 nm with varying grid parameters based on the spectral classification;  $T_{eff}$  (5500–6500 K in steps of 100 K), log  $g$  (4.0–4.5 in steps of 0.1), and  $v \sin i$  (20–50 km s<sup>-1</sup> in steps of 1 km s<sup>-1</sup>). The best fit model is with a  $T_{eff}$  of 5900 K, log  $g$  of 4.2, and  $v \sin i$  of 21 km s<sup>-1</sup>; see Appendix B for the  $\chi^2$  minimization results and Fig. 2 for the best fit and sensitivity of the spectrum to changes in effective temperature. The  $T_{eff}$  value is typical for G2-type pre-MS stars (Pecaut & Mamajek 2013) and the gravity is in agreement with luminosity class V.

Similar to Woitke et al. (2016) and Valegård et al. (2021), the Kurucz-model spectrum was fitted to optical photometry to determine the star’s luminosity, radius, extinction parameters, and log  $g$  from the spectral energy distribution (SED) fit. The results are reported in Tab. 1. The optical photometry is known to vary (see e.g., Torres et al. 1995; Rojas et al. 2008; Zacharias et al. 2009; da Silva et al. 2009; Kiraga 2012); therefore, we selected the mean V-band measurement of the ASAS-SN survey with 279 measurements over a period of five years in order to account for the variations ( $\Delta V \sim 0.43$  mag, Jayasinghe et al. 2018). A similar B-band study for PDS 111 is lacking. We used Gaia

magnitudes to inspect the behavior of  $B-V$ , applying Gaia photometry conversion tables from Busso et al. (2022). The mean  $B-V$  is 0.729 mag and varies with 0.075 mag. Although these variations are significant compared to the average errors on the  $B-V$  (<1%), we neglected color variability for our use because the absolute variations of the V-band were substantially higher. Therefore, we used the mean  $B-V$  from Gaia to obtain a B-band photometric point for the SED fit. For the fitting procedure, we fixed the distance to the Gaia distance from DR3<sup>2</sup> (Gaia Collaboration 2022) and effective temperature. The SED fit can be found in Appendix C, which shows an infrared excess compared to the stellar SED. We might observe excess flux compared to the bluest photometric point from SDSS in the u-band ( $\lambda_{eff} = 360.804$  nm), but more photometry blueward from the u-band is needed to confirm this. We used the variability of the V-band magnitude in the ASAS-SN survey, extinction, effective temperature, distance, and bolometric correction from Pecaut & Mamajek (2013) to infer errors on the luminosity and radius.

The luminosity and  $T_{eff}$  of the star result in a radius of  $1.52 R_{\odot}$ . Alternatively, the radius was derived from the  $v \sin i$ , rotation period, and inclination of the star. The TESS photometry displays a dominant period with the use of a Lomb-Scargle periodogram (Lomb 1976; Scargle 1982) of 3.137 days. This period is often attributed to the rotation period of the star. Using this period, the  $v \sin i$  of 21 km s<sup>-1</sup> from Kurucz model fitting and an inclination of 58° (see Sec. 3.3), we calculated a radius of  $1.53 R_{\odot}$ , which is within errors similar to the derived radius from the SED fit.

### 3.2. Scattered light observations

Our SPHERE H-band observations reveal an extended disk seen in polarized scattered light. We traced disk signal out to  $\sim 1''$  from the central star along the major axis of the disk, corresponding to  $\sim 158$  au. We show the SPHERE polarized and total intensity reductions in Fig. 1. The polarized light image shows a classical flaring disk with an illuminated top side, a dark mid-plane and an illuminated outer edge of the disk bottom side (going from North to South in the image). The disk is seen at an intermediate inclination. Tracing of the outer edge of the top side of the disk by eye yielded an inclination of  $\sim 60^\circ$  at a position angle (PA) of the major axis of  $\sim 68^\circ$ .

The total intensity image in Fig. 1 traces sub-structures on the disk top side. The employed angular differential imaging processing removed most of the signal with low spatial frequencies due to image self-subtraction (see e.g., Milli et al. 2012; Ginski et al. 2016; Stapper & Ginski 2022). We identified four pairs of arc-like structures, which indicate the presence of rings on the disk surface. As discussed in Ginski et al. (2016) the shape of these arcs is likely distorted due to the same image self-subtraction effects that filtered out the low spatial frequency data. In the rightmost panel of Fig. 1 we overlaid the contours of the total intensity image on the polarized light image which does not suffer from distortions of the disk morphology. The brightest pair of arcs in total intensity is tracing the outer edge of the disk top-side, while the two pairs of arcs further North trace rings in the inner part of the disk, also visible in the polarized light data. The faintest and southernmost pair of arcs in total intensity is tracing the edge of the disk mid-plane.

<sup>2</sup> The Renormalized Unit Weight Error (RUWE) is 2.6 which is discussed in Sec. 4.1.

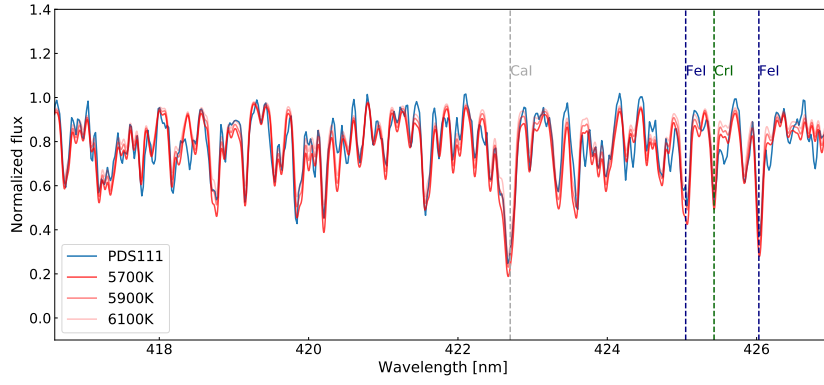


**Fig. 2.** The stacked spectrum of PDS 111 is shown together with a subset of Kurucz models with different temperatures. The models have a  $\log g$  of 4.2 and a  $v \sin i$  of  $21 \text{ km s}^{-1}$ .

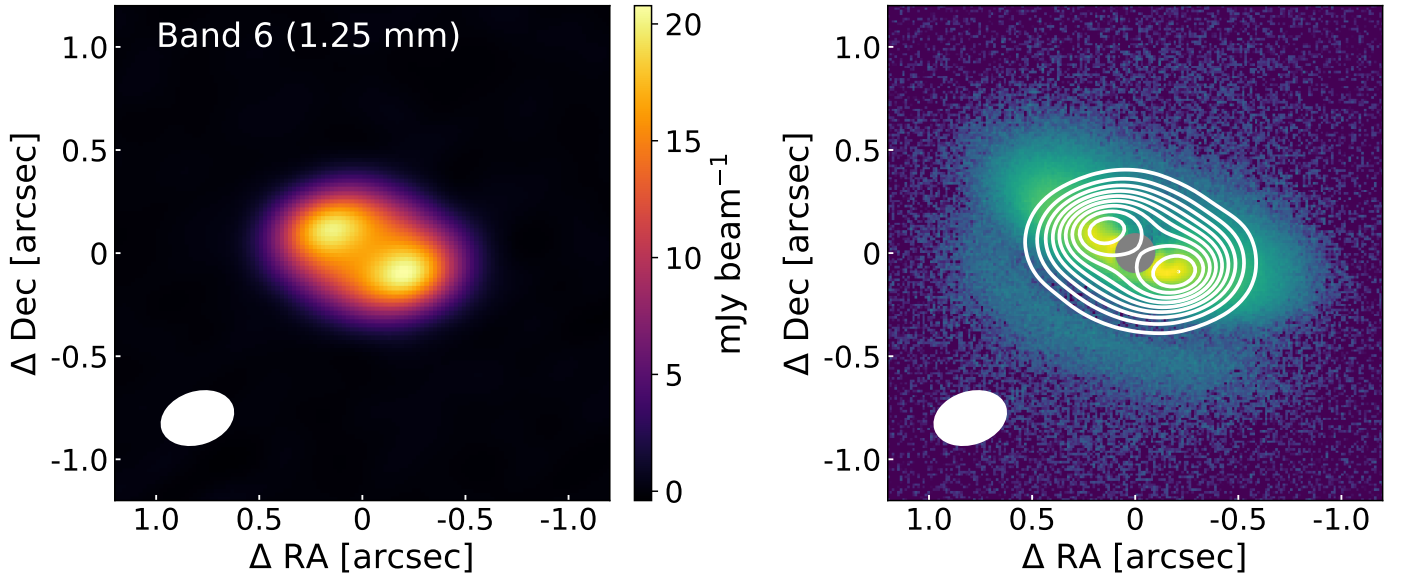


**Fig. 3.** ALMA observations of PDS 111. Left panel: Dust continuum emission at 1.25 mm of PDS 111. The resolution of the observations is  $0.357'' \times 0.25''$  with a position angle of  $-71.9^\circ$  and is shown in the lower left part of the figure. Right panel: Overlap of ALMA (contours at 10,...,100% of the peak of emission) and SPHERE observations (in color).

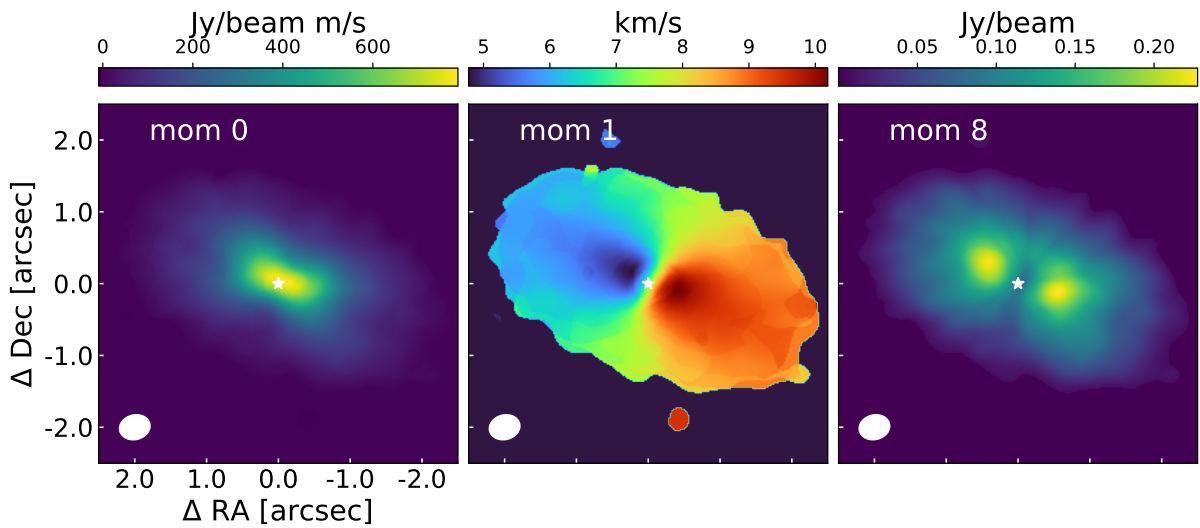


**Fig. 4.** Moment 0, 1, and 8 of the  $^{12}\text{CO}$  of PDS 111. Moment 0 (left) is the integrated value of the spectrum, moment 1 (middle) the intensity weighted coordinate to get the velocity dispersion and moment 8 (right) shows the peak value of the spectrum. The beam size is  $0.429'' \times 0.342''$  with a PA of  $-76.114^\circ$ , shown as the oval in the lower left corner of the panels.

### 3.3. Dust and line observations

#### 3.3.1. Dust continuum emission

Fig. 3 shows the dust continuum emission observed with ALMA with a final beam of  $0.357'' \times 0.25''$  with a PA of  $-71.9^\circ$  at 1.25 mm after self-calibration as described in Sec. 2.3. To check if the emission is optically thin, we calculated the optical depth of the peak of the continuum by assuming (e.g., Dullemond et al. 2018):

$$I_\nu(r) = B_\nu(T_d(r))(1 - \exp[-\tau_\nu(r)]) \quad \text{thus} \\ \tau = -\ln\left(1 - \frac{I(r_{\text{peak}})}{B(T_d(r_{\text{peak}}))}\right), \quad (1)$$

with  $T_d$  being the dust temperature at the peak location ( $r_{\text{peak}}$ ). Assuming a dust temperature of 20 K, the optical depth at the peak is  $\tau_{\text{peak}} = 0.27$ , similar to the values found in the DSHARP sample (Huang et al. 2018; Dullemond et al. 2018). This value of the optical depth may be underestimated because dust scattering could be neglected (Zhu et al. 2019), which would result from unresolved substructures in the ring, and/or a lower dust temperature or the large beam size relative to the disk.

If the emission is optically thin, the dust disk mass can be calculated as

$$M_{\text{dust}} \simeq \frac{d^2 F_\nu}{\kappa_\nu B_\nu(T)}, \quad (2)$$

where  $d$  is the distance to the source,  $F_\nu$  is the total flux at 1.3 mm, and  $B_\nu$  is the black-body surface brightness at a given temperature (Hildebrand 1983). Taking for the mass absorption coefficient  $\kappa_\nu = 2.3 \text{ cm}^2 \text{ g}^{-1} \times (\nu/230 \text{ GHz})^{0.4}$  (Beckwith et al. 1990; Andrews et al. 2013), we calculated a dust disk mass of  $45.8 M_\oplus$  or  $\sim 0.14 M_{\text{Jup}}$ , similar to typical disks around T Tauri stars in different star-forming regions (e.g., Pascucci et al. 2016).

#### 3.3.2. $^{12}\text{CO}$ emission

Fig. G.1 presents the channel maps of  $^{12}\text{CO}$  of PDS 111 observed with ALMA, showing emission from  $\sim 0.4 \text{ km s}^{-1}$  to  $\sim 14.7 \text{ km s}^{-1}$ . For comparison, the  $5\sigma$  level of the continuum emission is overplotted, and it shows that  $^{12}\text{CO}$  is more extended than the dust continuum emission and the scattered light detection.

Fig. 4 shows the moment 0, 1, and 8 (peak value of the spectrum) of the  $^{12}\text{CO}$  of PDS 111 generated with a Keplerian mask and clipping at  $3\sigma$  of the JvM corrected image as described in Sec. 2.3 (the beam size is  $0.429''$  or  $0.342''$  with a PA of  $-76^\circ.114$ ). To extract the stellar mass from the  $^{12}\text{CO}$  Keplerian rotation pattern, we used eddy<sup>3</sup>, <https://eddy.readthedocs.io/en/latest/> (Teague 2019), which gives  $1.29_{-0.18}^{+0.82} M_\odot$  when assuming a simple disk model and fixing the inclination to be that of the continuum. The large uncertainty in the stellar mass may come from the unknown vertical structure and disk orientation. Higher angular resolution is needed to better resolve the surface height with ALMA.

## 4. Age and disk properties

By combining the observations at different wavelengths, we are able to sketch a more complete picture of the system. Fig. 5

<sup>3</sup> Tool to extract kinematic information from spatially and spectrally resolved line data

shows what different parts of the disk are traced by the different observing techniques.

### 4.1. Age

Using the luminosity and effective temperature, we placed the star in the Hertzsprung Russell Diagram (HRD) on evolutionary tracks from Siess et al. (2000), and infer an age of 15.9 Myr and a evolutionary mass of  $1.20 M_\odot$ , see Fig. 6. The error on the effective temperature and conservative error on the luminosity lead to an uncertainty range of 12.2 – 17.6 Myr for the age and  $1.15 - 1.30 M_\odot$  for the mass. The mass is similar to the best fit mass value obtained in Sec. 3.3. Additionally, using the radius and surface gravity of the star in Tab. 1, we measured the spectroscopic mass. Using the  $\log g$  from the SED fit resulted in a mass of  $1.14 M_\odot$  and using the  $\log g$  from the spectrum fit resulted in a mass of  $1.34 M_\odot$ . Both are within the errors consistent with the evolutionary mass.

Manara et al. (2013) show that the age of T Tauri stars could be over-estimated when the extinction, accretion, and PMS stellar models are not fitted simultaneously. However, their method cannot be applied to PDS 111 since their stellar models go up to spectral type G4. The accretion rate is measured from line luminosities in Sec. 4.6 demonstrating that the accretion rate for PDS 111 is low for a star of this mass (Manara et al. 2023).

The estimated age of the system of 15.9 Myr could be wrong if the distance to PDS 111 obtained from the *Gaia* DR3 parallax (Gaia Collaboration 2022) is not correct. This may be the case considering the large RUWE value of 2.6, despite the small error on the parallax (0.035 mas). The RUWE statistic shows whether a single-star light profile fits the observations. The circumstellar material of PDS 111 might inflate its value. Fitton et al. (2022) determine that for disk-bearing sources a RUWE cutoff value of 2.5 is more appropriate. The RUWE value of PDS 111 is slightly above this cutoff<sup>4</sup>. We checked the *Gaia*-database to see whether the `visibility_period_used` is more than 10 and `ipd_gof_harmonic_amplitude` is less than 0.1. Both is the case: the former is 22 and the latter is 0.029. Moreover, the *Gaia* parallax cross-matches that obtained with *Hipparcos* (Gaia Collaboration 2022; ESA 1997). Therefore, we do not find any obvious indications that the *Gaia* measurements are inaccurate.

Throughout the SED fitting procedure, the total-to-selective visual extinction  $R_V$  is fixed to 3.1 (Cardelli et al. 1989). However, it has been noticed that  $R_V$  is sometimes higher toward star-forming regions (e.g., Ramírez-Tannus et al. 2017). If this value would for example be 4.1, the extinction toward the source would be higher and the luminosity would increase to a value of  $3.6 L_\odot$  and the corresponding age in the HRD would be 11.3 Myr for the same temperature, lowering the age of the system. More simultaneous photometric measurements over a period of time could help to improve the SED fit and fit for a range of different  $R_V$  values in order to find the best fitting parameter in the sightline of PDS 111. We conclude that the uncertainty in distance or extinction does not reject our hypothesis that PDS 111 is relatively old, that is at least  $\sim 11$  Myr. This relatively old age is similar to what has been determined for the stars that are surrounded by a "Peter Pan Disk"; we further discuss this scenario in Sec. 5.6.

<sup>4</sup> The circumstellar disk may inflate the RUWE value.

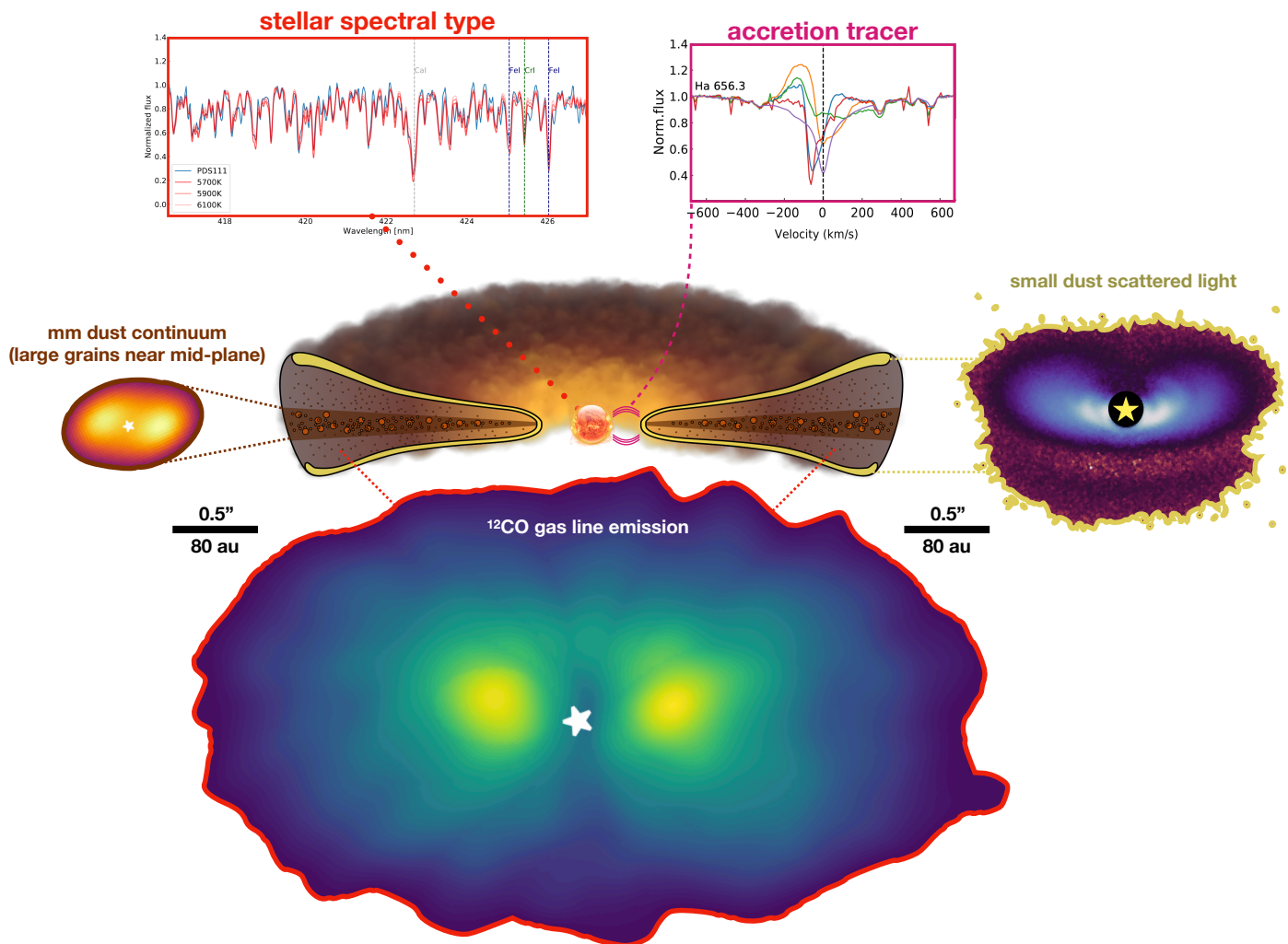


**Fig. 5.** Overview of PDS 111 indicating the parts of the system that are traced by the different observational techniques.

#### 4.2. Disk surface

As discussed in [de Boer et al. \(2016\)](#), [Ginski et al. \(2016\)](#), and [Avenhaus et al. \(2018\)](#), we used the identified disk sub-structures to extract the height profile of the disk surface layer at which the disk becomes optically thick for NIR radiation. To facilitate the tracing of the structures we employed high pass filtering as well as deconvolution techniques using the Adaptive Image Deconvolution Algorithm (AIDA) code by [Hom et al. \(2007\)](#). We show the high-pass filtered and the de-convolved data in [Fig. E.1](#) in [Appendix E](#). Because the disk structure is complex, we traced the individual rings by eye as was done by [Avenhaus et al. \(2018\)](#) for the case of IM Lup. Tracing was done for all structures in the original polarized light images, in the high-pass filtered images and in the de-convolved images to ensure that there was no mismatch in structures. To reduce the number of free parameters, the inclination of the individual rings as well as their PA were fixed to the values extracted from the ALMA data discussed in [Sec. 3.3](#). Thus, for each ring we traced an ellipse by re-scaling to match the semi-major axis and then applying an offset along the disk minor axis to match the height profile of the disk. Our results are shown in [Fig. 7](#) (top). Additionally we show a saturated image of the disk for the overlay of the ellipse on the outer disk edge in [Fig. E.2](#).

We overlay the resulting ellipses on the polarized light image and calculate the disk aspect ratio from the ellipse center-offset along the minor axis and the ellipse semi-major axis following [de Boer et al. \(2016\)](#). We find a steep increase in the disk aspect ratio from the innermost ring at 37 au to the second ring at 52 au from 0.12 to 0.26. While the aspect ratio of the inner ring is compatible with results presented by [Avenhaus et al. \(2018\)](#) for a small sample of T Tauri stars, the subsequent structures all show a higher aspect ratio, indicative of a strong flaring geometry of the disk, see [Fig. 7](#) (bottom). In addition to the two rings at 37 au and 52 au we identify a third more diffuse ring-structure in the deconvolved and high-pass filtered images (see [figure E.1](#)) at a separation of 74 au. Since this structure is of lower spatial frequency than the inner two rings it is entirely filtered out by the ADI post-processing and thus not visible in the total intensity image in [Fig. 1](#). We tentatively overlay an ellipse on this ring as well and find an aspect ratio of 0.23, roughly consistent with the inner ring at 52 au, however, with larger uncertainties.

The increase of the aspect ratio between the innermost ring at 38 au and the outer disk edge at 140 au, for which we found a value of 0.26, is in principle compatible with the extreme flaring profile found for the disk around the Herbig star HD 97048 by [Ginski et al. \(2016\)](#). However, since the aspect ratio at intermediate separations from the central star appears to be significantly higher, we could not fit the entire surface height profile with a

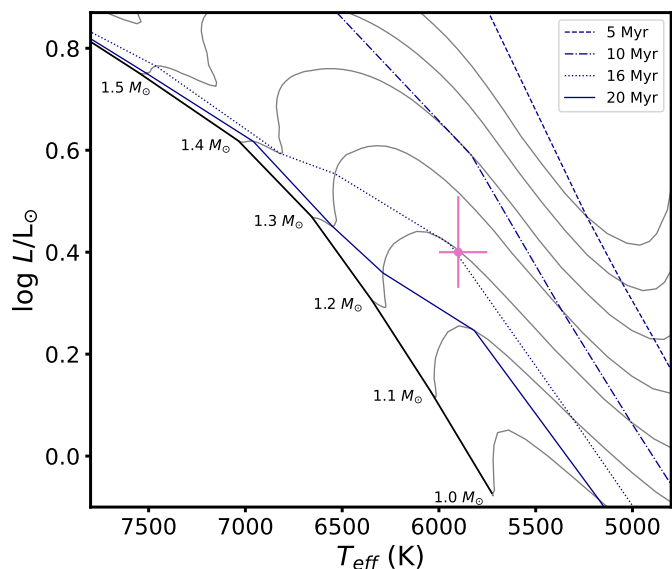


**Fig. 6.** Hertzsprung-Russell diagram with PMS tracks and isochrones from [Siess et al. \(2000\)](#). The location of PDS 111 coincides with an age of  $15.9^{+1.7}_{-3.7}$  Myr.

single power law. As briefly discussed in [Ginski et al. \(2016\)](#), this may be due to an optical depth effect, disproportionately affecting the outer disk region. As the dust density in the outer disk decreases, the optically thick layer sinks closer to the mid-plane.

#### 4.3. Disk asymmetry

For a disk with an azimuthally homogeneous dust and gas distribution, we would expect that the polarized light image is symmetric with respect to the disk’s minor axis. However, this does not appear to be the case for PDS 111. To highlight the disk asymmetry we flipped the image around the minor axis and then divided the original image by the flipped image. This highlights the areas in which both sides of the disk deviate. We show the result in Fig. 8. We see two main effects; first of all the disk is indeed asymmetric with flux deviations of up to a factor two between both sides. Second, we find a flip in the asymmetric brightness distribution (the white line between the red and blue areas) around  $0.3''$  (47 au) along the major axis. Inside of this border the North-East (NE) side of the disk is fainter than the South-West (SW) side, while it is the opposite way in the outer disk.

Since the SPHERE observations are tracing scattered stellar light, the disk brightness is intricately linked to the disk height profile and geometry. Broad brightness asymmetries as observed here can be caused by warps or misalignment in inner disk regions and subsequent shadowing of the outer disk (e.g., [Debes et al. 2017](#); [Benisty et al. 2018](#); [Muro-Arena et al. 2020](#)). In such a scenario the breaking or warping point would be at the location where we observe the flip in the asymmetric signal of the disk. In that case, the scale height inside of the flipping point would be increased in the SW on the disk top and decreased in the NE. This could then explain simultaneously why the disk is brighter inside the flipping point (it is more exposed to stellar light) and fainter outside the flipping point (the outer disk is shadowed by the inner disk) in the SW.

However, we note that in a warping scenario we would expect that the disk bottom side shows the opposite behavior from the disk top side, that is, we would expect the disk bottom side

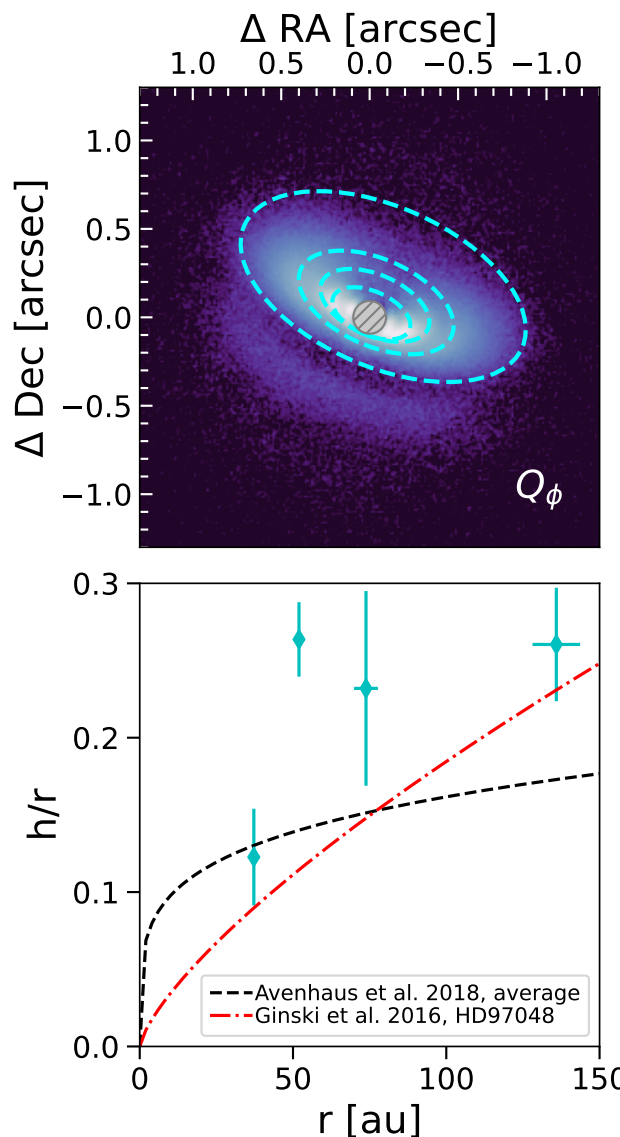


**Fig. 7.** Ellipses fitted to the radial sub-structures traced in scattered light (top) and resulting height of the scattering surface of the disk (bottom). We compare the scattering surface height with the average surface height profile of several T Tauri stars found by [Avenhaus et al. \(2018\)](#) and the extreme flaring case of the Herbig star HD 97048, discussed by [Ginski et al. \(2016\)](#).

to be bright in the SW. While the S/N is lower on the disk bottom, it nevertheless appears that it instead exhibits the identical behavior as the disk top side, which means it is faint in the SW and bright in the NE. This may then indicate that the disk is not radially warped or misaligned as a whole but rather shows a local change in scale height, symmetric around the disk mid-plane. This may be compatible with the fact that we are measuring an increased aspect ratio for the disk ring at 52 au. However, since we traced the ring at all azimuthal angles simultaneously a localized effect may be averaged out.

#### 4.4. Disk structure

The dust continuum emission morphology was analyzed with a parametric brightness modeling using the packages `galario` ([Tazzari et al. 2018](#)) to calculate the Fourier Transform of the



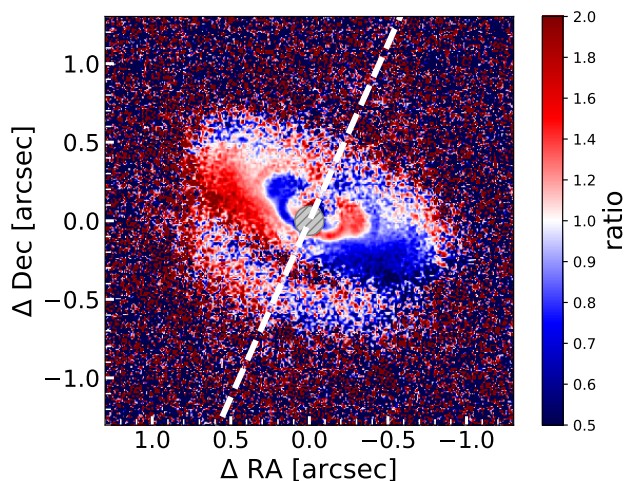


**Fig. 8.** The scattered light disk flipped around the minor axis and divided. The minor axis is indicated by the white, dashed line. The scattered light disk is asymmetric relative to the minor axis. The colorbar gives the flux ratio between the two sides of the disk, showing that the flux deviates up to a factor of two between both sides. Notably, the flux ratio turns around for the region inside of  $\sim 0.3''$  along the major axis. This may indicate a local change in scale height symmetric around the disk midplane rather than a warp or misalignment since the bottom side displays a similar flux ratio.

models and zeus (Karamanis & Beutler 2020; Karamanis et al. 2021) to run an MCMC and sample the posterior likelihood of the parameter space. We considered four components to describe the PDS 111 emission: A centrally peaked Gaussian ( $g_1$ ) motivated by the inner emission found in several single-ringed disks (e.g., Pinilla et al. 2021; Pyerin et al. 2021), two Gaussian profiles for the ring ( $g_2, g_3$ ) to allow for radially asymmetric ring morphology (rather than one broken Gaussian profile), and a Gaussian azimuthal asymmetry ( $g_4$ ) to describe the over-emission observed in the South-western side of the disk. Fig. F.1 illustrates each of the components of the model used to fit the morphology of PDS 111. We also include as free parameters the central position of the disk ( $x_0, y_0$ ) and the geometry, given by inclination and PA. Every parameter has a flat prior and boundaries representative of physical limitations, such as only allowing positive distances and brightness. The model images have a pixel size of 4 mas and an image size of 2048 pixels. We ran the MCMC with eight times the number of parameters as the number of walkers ( $n_{\text{walk}} = 136$ ). For each walker, the burn stage was 5000, and 6000 for the parameter space sampling. The summary of the modeling results is given in Tab. 2.

Fig. 9 shows the comparison between the dust continuum observations and model images from our best fit with `galario` after convolving with the same beam as the observations and the residuals. The residual map demonstrates that our model recovers most of the morphology of the dust continuum emission. The main characteristic of the dust morphology is a cavity with a ring-like emission peaking at  $\sim 30$  au (see Fig. F.1 for the model components). The radius that encloses 90% of the total flux from the visibility fitting is  $\sim 55$  au.

#### 4.5. Radial extent of the disk

The radial distribution and extension of PDS 111 in dust continuum, scattered light and  $^{12}\text{CO}$  is shown in Fig. 10. For the ALMA profiles, the images have been deprojected and then az-

**Table 2.** Dust continuum visibility modeling results.

|                   | Property            | Best value $\pm 1\sigma$ | unit               |
|-------------------|---------------------|--------------------------|--------------------|
| Disks<br>Geometry | $x_0$               | $27.3 \pm 0.6$           | mas                |
|                   | $y_0$               | $7.4 \pm 0.3$            | mas                |
|                   | $inc$               | $58.2 \pm 0.1$           | deg                |
|                   | $PA$                | $66.2 \pm 0.1$           | deg                |
| $g_1$             | $f_1$               | $119.8^{+146.5}_{-94.4}$ | $\mu\text{Jy/pix}$ |
|                   | $\sigma_1$          | $3.8^{+4.9}_{-2.6}$      | mas                |
| $g_2$             | $f_2$               | $1.8^{+1.3}_{-0.9}$      | $\mu\text{Jy/pix}$ |
|                   | $r_2$               | $280.8^{+45.0}_{-28.0}$  | mas                |
|                   | $\sigma_2$          | $94.9^{+25.3}_{-21.9}$   | mas                |
| $g_3$             | $f_3$               | $22.1^{+1.4}_{-0.7}$     | $\mu\text{Jy/pix}$ |
|                   | $r_3$               | $286.6^{+2.6}_{-3.5}$    | mas                |
|                   | $\sigma_3$          | $33.8^{+4.7}_{-6.1}$     | mas                |
| $g_4$             | $f_4$               | $2.4^{+1.4}_{-0.7}$      | $\mu\text{Jy/pix}$ |
|                   | $r_4$               | $286.7^{+31.0}_{-54.2}$  | mas                |
|                   | $\sigma_{r4}$       | $116.5^{+4.7}_{-30.8}$   | mas                |
|                   | $\theta_4$          | $-175.2 \pm 2.4$         | deg                |
|                   | $\sigma_{\theta 4}$ | $11.3^{+3.6}_{-4.0}$     | deg                |
| Properties        | $F_{\text{tot}}$    | $139.1^{+0.2}_{-0.6}$    | mJy                |
|                   | $R_{68\%}$          | $307.2^{+2.5}_{-1.7}$    | mas                |
|                   | $R_{90\%}$          | $345.4^{+0.9}_{-5.8}$    | mas                |
|                   | $R_{95\%}$          | $376.6^{+5.9}_{-11.1}$   | mas                |

**Notes.** Uncertainties represent the 68% dispersion range. Pixel size was 4 mas. The central angle of the asymmetry ( $\theta_4$ ) is measured relative to the disk PA. The second column gives the properties of the four Gaussian model components; flux ( $f$ ), sigma ( $\sigma$ ), radius ( $r$ ), and asymmetry angle ( $\theta$ ).

imuthally averaged, while for the SPHERE data we show radial cuts at the North-East (NE) and South-West (SW) of the major axis of the disk. The vertical lines show the radius that encloses 90% of the emission in each of the maps. The 90% radius of the  $^{12}\text{CO}$  map ( $\sim 295$  au) is much more extended than that tracing the dust, both in scattered light and continuum emission. The 90% radius of the dust continuum emission is at 95 au, three times smaller than observed in  $^{12}\text{CO}$  (both profiles being affected by convolution of a similar beam). The latter is very similar to the average ratio observed in several protoplanetary disks that are on average younger (Long et al. 2022).

The radius that enclose 90% of the flux measured directly from the dust continuum emission (95 au) and that measured from the visibility fitting of the dust continuum emission (55 au, Sec. 4.4) are different. This is a natural result of the large ALMA beam and the high inclination of the source. The  $\sim 55$  au estimate is probably more representative of the actual size, therefore of the distribution of mm-grains that dominate the emission at ALMA wavelengths. Fig. 10 shows that this mm-grain thermal emission disk is smaller than the disk size from scattered light ( $\sim 105$  au for the NE and  $\sim 96$  au for the SW cuts), which would indicate that the small grains responsible for the scattering are more radially extended than the large grains, as a product

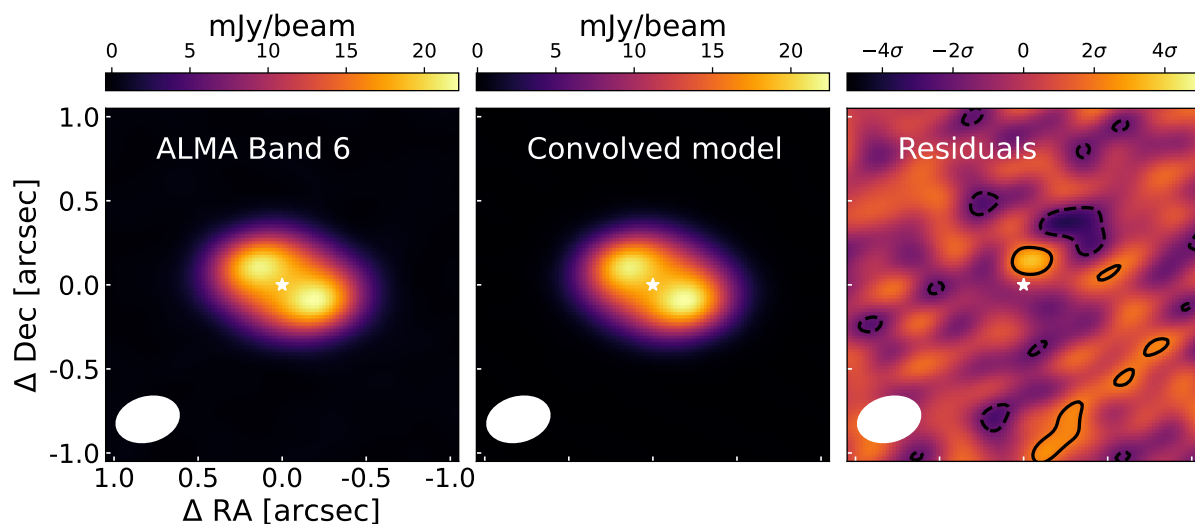


**Fig. 9.** Observations versus model images from our best fit with *galario* after convolving with the same beam as the observations and the residuals. The contours of the residual map are  $[-4\sigma, -2\sigma, 2\sigma, 4\sigma]$ , where negative values are dashed contours and positive values solid contours.

of radial drift (e.g., Guilloteau et al. 2011; Tazzari et al. 2016; Trapman et al. 2019, 2020).

When the radial profiles from scattered light are multiplied by  $r^2$  to compensate for the stellar illumination, the 90% radius shifts to  $\sim 155$  au for the NE and  $\sim 136$  au for the SW emission (in line with the 158 au mentioned in Sec. 3.2 at which the disk signal drops below the noise floor along the major axis). The size of the disk in scattered light is thus  $\sim 2.4$ - $2.7$  times larger than in the millimeter emission. Such a difference is similar to that found in the ALMA images of dust vs. gas emission. Trapman et al. (2019, 2020) propose that optical depth effects cannot explain such a big difference, and this is likely evidence for small and large grain separation through radial drift.

#### 4.6. Inner gaseous disk

The presence of hot gaseous circumstellar material is revealed by  $H\alpha$  and  $H\beta$  emission and strong variability in these and other  $H$  I, He I, Ca II and Na I lines. We do not detect any forbidden emission lines. The equivalent width (EW) is determined after subtracting the best fit Kurucz model from the observations. This ensures that the measured EW is an indication of the emission or absorption from the circumstellar material. The EW measurements are listed in Tab. D.1. The  $EW(H\alpha)$  emission is  $< 10\text{\AA}$ , which classifies PDS 111 as a weak-line T Tauri star.

Following Alcalá et al. (2017), we determined line luminosities by measuring the EW of the lines, the absolute flux from the SED in  $H\alpha$  and  $H\beta$  and converting this to luminosity using the distance to the star. Their empirical relations were used to convert the line luminosities to accretion luminosities and the resulting mass-accretion rates assuming a typical inner radius of  $5 R_*$ , are reported in Tab. 3. This yields a rate that varies between  $1$ - $5 \times 10^{-10} M_\odot \text{ yr}^{-1}$ . Due to the lack of photometric observations in the UV, the mass-accretion rate could be constrained only indirectly.

The temporal variance method (TVS; Fullerton et al. 1996; de Jong et al. 2001) is employed to study spectroscopic variability. The observed standard deviation  $\sigma_{\text{obs}}$  is compared to the expected standard deviation  $\sigma_{\text{exp}}$  at a certain wavelength bin  $j$ . If the ratio of the two standard deviations exceeds unity, the variation in the spectral line between the epochs is larger than what is

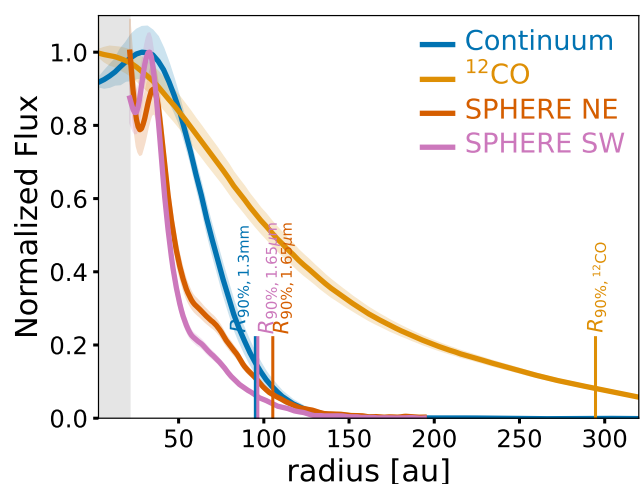


**Fig. 10.** Azimuthally averaged radial intensity profiles of the deprojected images from ALMA dust continuum and the moment 0 maps of the  $^{12}\text{CO}$  from ALMA Band-6 observations of PDS 111. Each profile is normalized to the peak. The ALMA profiles include the standard deviation of each elliptical bin divided by the square root of the number of beams spanning the full azimuthal angle at each radial bin. For the SPHERE observations, we take two radial cuts at the North-East (NE) and South-West (SW) of the major axis of the disk. The vertical lines show the radius that encloses 90% of the emission in each of the maps. The gray region shows the size of the coronagraph in the SPHERE observations.

**Table 3.** Derived mass-accretion rates of  $H\alpha$  and  $H\beta$  at each epoch in  $\log M_{\text{acc}} [M_\odot \text{ yr}^{-1}]$ .

| $\lambda_{\text{rest}}$ (nm) | 28-11-'21 | 07-12-'21 | 20-10-'22 | 28-10-'22 |
|------------------------------|-----------|-----------|-----------|-----------|
| $H\alpha$ 656.28             | -9.47     | -9.28     | -9.37     | -9.69     |
| $H\beta$ 486.14              | -9.42     |           | -10.02    | -9.42     |

expected from the noise in that wavelength bin. Likewise, when no variation is detected, the ratio (i.e., the value of the TVS)

is randomly distributed around unity, reflecting the noise in the data.

Similar to [de Jong et al. \(2001\)](#) and [Derkink et al. \(2024\)](#),  $\sigma_{\text{obs},j}$  is determined from the average of the standard deviations of the bins in the continuum region around the spectral line in all epochs. This yields  $\sigma_{\text{con}}$ , which is scaled by the ratio of the mean normalized flux of all epochs of the evaluated wavelength bin  $j$  and the continuum. The  $\sigma_{\text{obs},j}$  is calculated from observed fluxes in wavelength bin  $j$ . The TVS value is given by the ratio:

$$\text{TVS}_j = \frac{\sigma_{\text{obs},j}}{\sigma_{\text{exp},j}} = \frac{\sigma_j}{\sigma_{\text{con}}} \sqrt{\frac{\bar{F}_{\text{con}}}{\bar{F}_j}}. \quad (3)$$

Here  $\bar{F}_j$  is the average flux in wavelength bin  $j$  for all epochs and  $\bar{F}_{\text{con}}$  the average continuum flux. The significance of the variability is determined by comparing a  $\chi^2$ -distribution with the degrees of freedom set to the number of observations, to the TVS value. A 95% level is used for a significant detection.

The resulting TVS for all significantly varying lines are shown in [Fig. 11](#) and were used to measure the maximum velocity at which significant variability is detected. The lines that vary in a similar manner are shown together. The highest velocities and strongest variations are seen in H $\alpha$  and He I, up to 320 km s<sup>-1</sup> on the red side. The blue side shows variability up to 220 km s<sup>-1</sup> which is similar to the highest variable velocities on both sides of the other H I lines. Na I lines show variations up to 120 km s<sup>-1</sup> on the red side and up to 90 km s<sup>-1</sup> on the blue side. The latter is similar to that seen in the red side of the components of the Ca II triplet.

The circumstellar H $\alpha$  emission, after star model subtraction and radial-velocity correction, has a strongly varying line profile ([Fig. 12](#)). The first and last epochs are characterized by a strong and sharp absorption component around ~55 km s<sup>-1</sup> on the blue side of the feature. The second epoch shows an inverse P Cygni profile and the third is characterized by two emission peaks, one around the rest wavelength and the other blue shifted. These profiles are discussed in [Sec. 5.5](#).

#### 4.7. Binarity

We calculated the contrast curves for the angular differential imaging final imaging. Those have been calculated using the Principal Component Analysis method. Then we assumed an age for the system of 16 Myr and a distance of 158 pc. The contrast curves were converted in mass limits of putative companions around the object. The mass limits are shown in [Fig. 13](#).

We observe no obvious detection of an inner binary component in the SPHERE data. Specifically, we can rule out objects down to ~0.25 M<sub>⊙</sub> and down to the coronagraphic edge at 0.1'', that is 16 au.

With these limits, we calculate the maximum expected radial velocity shift in the spectrum of the primary for a secondary mass of 0.25 M<sub>⊙</sub>. At 16 au the radial velocity of the primary would be ~1 km s<sup>-1</sup>, which would increase to ~2 km s<sup>-1</sup> when the distance between the primary and secondary is 8 au and to ~5 km s<sup>-1</sup> for a separation of 1 au).

The mid-resolution X-shooter spectra and limiting signal-to-noise ratio of the HERMES spectra would be sufficient to detect radial velocity shifts down to at least 5 km s<sup>-1</sup> if the epochs would be taken at opportune moments. This would mean that we should detect a secondary mass of 0.25 M<sub>⊙</sub> if this star would have a separation < 1 au from the primary. The corresponding period of a few months at this separation is shorter than the time between the X-shooter and HERMES observations. Therefore,

given our imaging and spectroscopic detection limits, the disk could potentially be a circumbinary disk, hiding a low mass secondary companion of a few tenths of M<sub>⊙</sub> at a separation between ~1-16 au.

## 5. Discussion

### 5.1. A very flared, but old disk

One of the most intriguing properties of PDS 111 is the amount of flaring of the dust in the disk, which is comparable to systems that are much younger than PDS 111 ([Fig. 7](#)). If it is really this old, then such strong flaring suggests that vertical stirring of small grains is still efficient after ~16 Myr of evolution, implying that vertical turbulence remains at play. The origin and evolution of turbulence as well as the origin of small grains in protoplanetary disks is a matter of debate. Regarding turbulence, the traditional picture is that the magneto-rotational instabilities (MRI) would be the main source of disk turbulence, but the efficiency of MRI is a complex process that depends on dust properties and abundance, the magnetic field strength and configuration, the gas and dust chemistry, and various ionization sources (see recent review in PPVII by [Lesur et al. 2022](#)); most of these are not constrained by observations. Other hydrodynamical instabilities can contribute to vertical mixing, such as the vertical shearing instability (e.g., [Flores-Rivera et al. 2020](#); [Barraza-Alfaro et al. 2021](#)). In PDS 111, whatever is dominating the dust vertical mixing still needs to be efficient after ~16 Myr of evolution, and be comparable to much younger disks, such as the flared disk of IM Lup ([Avenhaus et al. 2018](#)). [Franceschi et al. \(2023\)](#) model this star and suggest that the flaring could be caused by small particles that do not settle, because they do not grow after an initial growth time scale; some remain at high altitude because of long collisional time scales.

An alternative explanation is that the disk around PDS 111 lacks turbulence and that the scattered light observations trace very small fluffy particles, which would not settle in the absence of vertical turbulence ([Dullemond & Dominik 2004](#); [Kataoka et al. 2013](#)). Such particles can remain in the surface layers of the disk for several Myr if they do not grow and do not become compact.

Another possible explanation is that the flaring is caused by small dust particles that are added to the disk surface by continuing infall on the disk surface or by blowing dust from the inner system to the disk surface. The possibility of infall from the surroundings to the disk ([Dominik & Dullemond 2008](#)) is explored in [Sec. 5.4](#), where we discuss the near environment of PDS 111.

We exclude a disk wind from causing the flared surface layer, as seen in RY Tau ([Valegård et al. 2022](#)). A wind would make the surface of the disk more smooth without observable substructures in SPHERE, which is not the case in PDS 111. We do observe hints of sporadic outflows (see [Sec. 5.5](#)), but we do not observe any forbidden emission lines in the spectrum often related to a disk wind ([Nisini et al. 2018](#)).

### 5.2. Origin of the observed millimeter-cavity

PDS 111 displays a shallow cavity in the dust continuum emission that peaks at 30 au, and which is not detected in scattered light or in the <sup>12</sup>CO emission because the emission is hot and optically thick, similar to what has been seen in larger samples of transition disks (e.g., [Villenave et al. 2019](#)). This cavity can originate from planet-disk interaction or (magneto-) hydrodynamical instabilities. In the case of planet-disk interaction, the planet

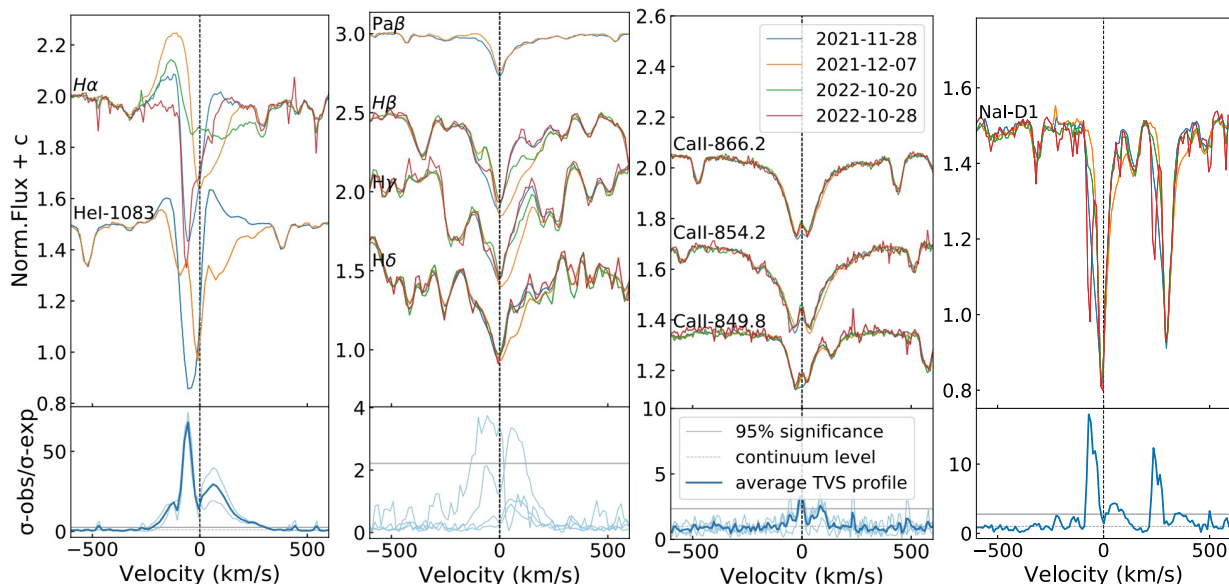


**Fig. 11.** Variable lines in PDS 111. From left to right:  $H\alpha$  and  $\text{He I } \lambda 1083.0$  nm lines in the spectra of PDS 111 are shown on velocity scale in the upper panel. They show significant variations. This is quantified in the lower panel by the use of the temporal variance spectrum, showing the significant variable velocity regime and similarity in the amplitude of the variation. The second panel shows three Balmer ( $H\beta$ ,  $H\gamma$  and  $H\delta$ ) lines and  $\text{Pa}\beta$ , all displaying variations. The variations are quantified in the lower plot of that panel, showing variations in a similar velocity range as in the lower left panel. The third panel shows the Ca II triplet, and the last panel the Na I doublet. The  $\text{He I } \lambda 1083.0$  nm and  $\text{Pa}\beta$  line only include two spectra due to the limited wavelength range of HERMES compared to X-shooter. The HERMES observation on 28-10-2022 shows strong telluric contamination.

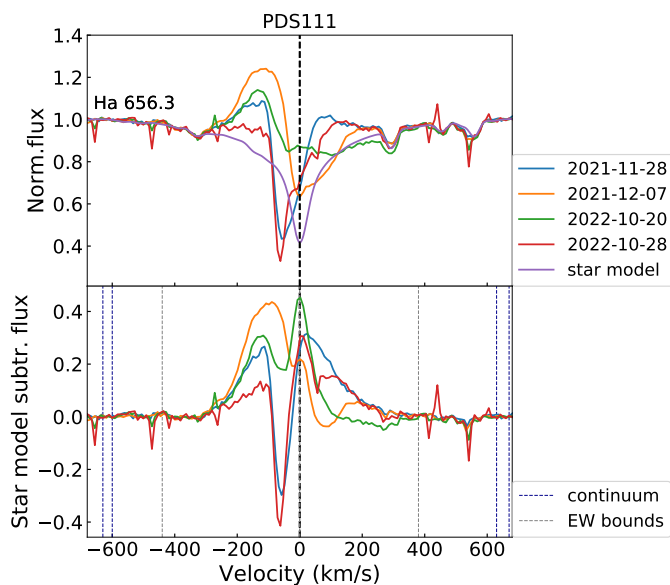


**Fig. 12.** The  $H\alpha$  line of PDS 111. The upper panel shows the  $H\alpha$  lines of the four epochs and a star model. This star model is used to subtract the stellar contribution to  $H\alpha$ . The result is shown in the lower panel. The blue and gray dotted lines are the intervals used for normalization and measuring the equivalent width.

mass should be  $\lesssim M_{\text{Jup}}$  because otherwise a cavity would have been opened in small grains and that would leave a signature in scattered light (de Juan Ovelar et al. 2013), and potentially in the  $^{12}\text{CO}$  (Facchini et al. 2018). The mass of such a planet would allow gas to flow through the gap maintaining mass-accretion onto the star (Zhu et al. 2011; Zhang et al. 2018), which is moderate in PDS 111 (Tab. 3). The detection of one or more planets is chal-

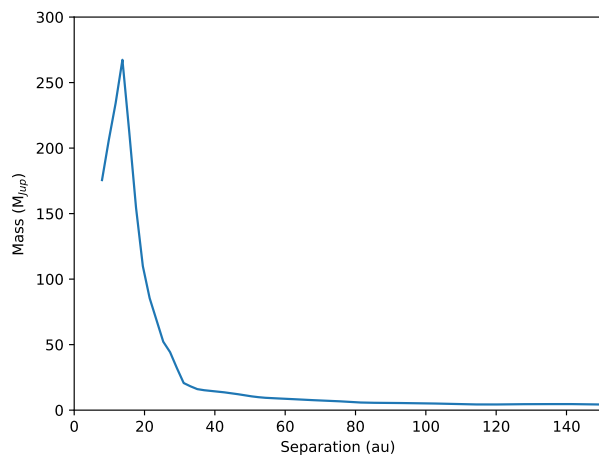


**Fig. 13.** Detectable minimum mass of co-eval (sub)stellar companions to PDS 111 based on our SPHERE data processed with angular differential imaging.

lenging with current telescopes (e.g., with JWST, Wagner et al. 2024) because of their potential location ( $\lesssim 30$  au) and low mass.

Alternatively, stellar binarity could also explain the presence of a cavity. Its shape depends on the mass ratio, eccentricity, and disk viscosity (e.g., Artymowicz & Lubow 1994; Miranda et al. 2017). The location of the ring in the binary case can be 3.5-4 times the binary separation. For PDS 111 that would be a binary separation around 8 au. The binary scenario is further discussed in Sec. 5.3.

Other origins of the cavity such as dead zones (e.g., Flock et al. 2015; Delage et al. 2022) cannot be excluded. More obser-

vational constraints, such as disk kinematics, may help to understand its origin.

### 5.3. Binarity

A circumbinary disk might explain several of the observed disk features such as the scattered light asymmetry, as well as the large disk cavity in the mm-continuum, as discussed in Sec. 5.2, for which the predicted separation is around  $\sim 8$  au. Binarity could also explain the high RUWE value. Juhász & Facchini (2017) performed 3D SPH hydrodynamic simulations of a disk warp induced by a central binary. The synthetic scattered light images show that a disk warp can create strong illumination asymmetries, due to disk shadowing, especially when the warp "axis" is aligned with the disk minor axis. However, we note that their Fig. 5 (panel p) shows that for a continuous warp we would expect the illumination pattern to be reversed between disk top and bottom side. As we discuss in Sec. 4.3, this does not appear to be the case in PDS 111, which may indicate a local increase in scale height rather than a continuous warp.

Recent SPH hydrodynamic models by Ragusa et al. (2020), Muñoz & Lithwick (2020) and Penzlin et al. (2022) suggest that a circumbinary disk that is co-planar with the orbital plane will always develop an eccentricity even if the initial binary orbit was close to circular. The main condition that they find is that the mass ratio between the binary components is  $q > 0.05$ . This means in the case of PDS 111 a binary component more massive than  $55 M_{\text{Jup}}$  would be required. This is not ruled out by our detection limits. Following the relation between cavity size and binary orbit recovered by Ragusa et al. (2020), we would expect the binary component to be located at a semi-major axis of  $\sim 8.5$  au. This is again consistent with our detection limits. However, we note that the presence of such a massive perturber at this relatively large separation might be in tension with our non-detection of the disk cavity in small grains, that is scattered light.

Ragusa et al. (2020) find that their disks become increasingly eccentric because of resonant excitation or periodic "pumping" via oblique spiral shocks (Ogilvie 2008; Shi et al. 2012). Due to the eccentricity, a "traffic jam" makes the density of the gas and dust higher at the apocenter than at pericenter (Ataiee et al. 2013; Ragusa et al. 2020), potentially explaining the observed asymmetries in PDS 111, as well as the possible local puffed up disk in scattered light.

The ALMA data puts an upper limit on a potential cavity gap size caused by a stellar companion. If there is a gas cavity, we would have detected this in the gas emission if the cavity was larger than the beam size of the  $^{12}\text{CO}$  measurement, like in CS Cha (Kurtovic et al. 2022). Therefore, the cavity must be smaller than  $0.429''$ .

Literature only shows a few confirmed cases of prominent young, circumbinary disks seen with SPHERE, for instance HD 142527 (Fukagawa et al. 2006; Biller et al. 2012; Close et al. 2014), HD 34700 (Monnier et al. 2019) GG Tau (Roddi et al. 1996; Keppler et al. 2020), and CS Cha (Ginski et al. 2018). In most of these cases, the resolved scattered light disk shows strong azimuthal asymmetries like spiral arms, which are not in our observations of PDS 111. However, this may strongly depend on the binary separation, eccentricity, mass ratio, and orbit inclination relative to the disk. We note that in the case of the CS Cha circumbinary disk the outer scattered light disk appears completely smooth and featureless, highlighting the diversity in disk morphology.

### 5.4. Environment

PDS 111 is known to be a foreground star of the Orion cloud (Torres et al. 1995), recently also confirmed by its *Gaia* DR3 distance ( $\varpi = 6.3136 \pm 0.0352$  mas; Gaia Collaboration 2022). No strong arguments are found that suggest the star is a member of a young cluster. PDS 111 has been associated with the Columba association (Torres et al. 2008; da Silva et al. 2009; Launhardt et al. 2022). However this predates the availability of an accurate trigonometric parallax measurement (Tycho parallax was  $\varpi = 28.70 \pm 21.60$  mas; ESA 1997). Columba is, however, older ( $42_{-4}^{+6}$  Myr; Bell et al. 2015) and an early G-type member would already be on the main sequence. The amount of circumstellar matter and our evolutionary age imply PDS 111 is considerably younger. Another membership assignment from the literature is with Theia 160 (Kounkel & Covey 2019), a clumpy string of co-distant and co-moving stars associated with PDS 111. This string shows young stars, but also includes stars that have been attributed to a much older ( $62 \pm 7$  Myr) group, the  $\mu$  Tau association (Gagné et al. 2020). More investigation into the young stars associated with Theia 160 could lead to a PMS track age, which would give additional constraints on the age of the star. So, its genetic connection to any characterized young stellar groups is uncertain at present.

Furthermore, its environment could be important for a rejuvenation scenario, where streamers feed material to the disk (Kuffmeier et al. 2020; Ginski et al. 2021). Arc-like structures, spiral arms, disk misalignment, or other disk structures in later stages of star formation, might be related to late infall of material to the disk. Therefore, late infall could have influenced the flaring and asymmetry in the disk of PDS 111. The STILISM 3D maps (Lallement et al. 2018) predict reddening toward PDS 111 at distance of 158 pc to be very modest  $E(B-V) = 0.008 \pm 0.016$  mag ( $A_V = 0.025 \pm 0.050$  mag), and the reddening is not expected to exceed  $E(B-V) \sim 0.05$  mag until  $\sim 475$  pc (i.e., near Orion complex), so there does not seem to be any dense, high extinction interstellar dust clouds in its vicinity. Given its disk, any significant reddening or changes in reddening must be due to its own circumstellar disk. Therefore, it seems unlikely that the disk is rejuvenated by its local environment.

### 5.5. $H\alpha$ and $\text{He I}$ variability

The hot gas from which  $H\alpha$  originates is highly variable in line morphology and shows velocities up to  $320 \text{ km s}^{-1}$ . These velocities, assuming a Keplerian rotating disk, are formed close to the stellar surface. The inverse P Cygni profile, seen in the epoch of 2021-12-07, is widely interpreted as a signature of accretion (e.g., Cauley & Johns-Krull 2014) and has a red-shifted absorption component in the feature around  $\sim 100 \text{ km s}^{-1}$ . The deep narrow blue-shifted absorption component in the first and last epoch is strongly variable and resides at relatively low velocities ( $< 100 \text{ km s}^{-1}$ , Nisini et al. 2018; Bouvier et al. 2023). This  $\text{He I}$  feature shows a similar blue-shifted absorption feature in the one epoch that also has an X-shooter observation. Since the blue-shifted absorption is deep, narrow and variable, it probably arises when some cooler optically thick material moves in front of the hot gas from the inner disk where the  $H\alpha$  and  $\text{He I}$  lines are formed. These blue-shifted features are generally associated with outflows (Kwan et al. 2007; Nisini et al. 2018; Bouvier et al. 2023).

Cauley & Johns-Krull (2014) observed similar profiles in a large sample of  $\text{He I}$  emission lines from PMS stars and imply an origin of the line morphology from a misalignment between the

inner and outer disk. [Bouvier et al. \(2023\)](#) also showed a similar line morphology of the He I and Balmer lines in the classical T Tauri star GM Aur with a mass accretion rate of  $\sim 10^{-8} M_{\odot} \text{ yr}^{-1}$  and an inclination of  $\sim 68^{\circ}$ . By combining optical and NIR photometry, and high-resolution spectroscopic time series, they concluded that these line features are caused by sporadic mass loss from the disk surface. The blue-shifted narrow absorption components in GM Aur start at high velocities, move to lower velocity over a period of days and disappear. Whether PDS 111 shows similar mass loss or an inner-disk misalignment is to be confirmed by follow-up observations with a higher time cadence (e.g., daily).

### 5.6. Long-lived accretion disks

Recently, [Silverberg et al. \(2020\)](#) found a class of long-lived accretion disks around M-dwarfs with ages above 20 Myr, so-called "Peter Pan disks" for their refusal to "grow up" and disperse. They concluded that these disks were most likely gas-poor hybrid disks, exhibiting signs of young and debris disks, but could not explain why such old systems still harbored these disks. [Coleman & Haworth \(2020\)](#) used disk evolutionary models to study possible conditions for a gas-rich disk to survive around these old stars. They concluded that a low turbulence parameter  $\alpha \sim 10^{-4}$ , a high initial disk mass ( $>0.25 M_{*}$ ) and very low external photo-evaporation ( $<10^{-9} M_{\odot} \text{ yr}^{-1}$ ) can reproduce the "Peter Pan disks" around M-dwarfs. Importantly, they also studied how these conditions would change for higher central star masses, as would be the case for the PDS 111 system. They conclude that for a solar mass star, a disk can be maintained up to 50 Myr under similar conditions, if external photo-evaporation is extremely low ( $<10^{-10} M_{\odot} \text{ yr}^{-1}$ ).

### 5.7. A coherent picture of the disk of PDS 111

We speculate that both radial and azimuthal sub-structures could be caused by an internal perturber. Either a low-mass planet close to the cavity edge at  $\sim 30$  au, which may explain the continuum cavity as well as the absence of such a cavity in the gas or scattered light, or a close-in stellar binary located between 1.5 and 16 au, with a preference for 8.5 au to explain the mm cavity size. Such a binary may then also explain the azimuthal asymmetry by exciting disk eccentricity. The presence of a perturber in the disk cavity might also go some way to explain the presence of a gas-rich disk at the old age of the system by trapping material in the outer disk. This may be consistent with the low accretion rate of  $1.5 \times 10^{-10} M_{\odot} \text{ yr}^{-1}$  that we inferred from our H $\alpha$  and H $\beta$  measurements. Still, planet formation and thus cavity opening is presumably a common occurrence in young disks. Related sub-structures are indeed detected in numerous systems with high-resolution ALMA or scattered light observations (e.g., [Andrews et al. 2018](#); [Benisty et al. 2023](#)). Yet studies that measure the disk occurrence rate in young clusters typically find that most disks have dispersed after 10 Myr (e.g., [Mamajek 2009](#); [Fedele et al. 2010](#); [Ribas et al. 2014](#)).

## 6. Summary and Conclusions

We present the results of an extensive observational campaign of the hitherto relatively unexplored PDS 111 system in the framework of the DESTINYs program. Our spectroscopic, imaging and mm-interferometry observations explore the system from the stellar photosphere out to the edge of the gaseous disk at

$\sim 295$  au. They reveal a system that appears archetypal in many ways for a young gas-rich circumstellar disk. Yet our spectroscopic analysis of the central star as well as the possible membership in the Columba association place the system age at an age of  $\sim 16$  Myr (for spectroscopy) or even significantly older (for association membership). Equally puzzling is the relative isolation of PDS 111 in the foreground of the Orion star-forming region.

Our NIR scattered light observations as well as ALMA continuum observations resolve the outer disk and reveal radial sub-structures as well as azimuthal asymmetries. The azimuthal asymmetry might trace a warp or local overdensity in the outer disk. Interestingly, the complex and variable profiles of the H $\alpha$  line might also indicate a misalignment of the inner disk region.

The "Peter Pan disk" scenario for higher mass central stars fits well with the relative isolation of PDS 111. Thus it is possible that the combination of low external photo-evaporation due to lack of close association neighbors as well as the cavity opening and subsequent low viscous transport of material within the disk conspired in this system to maintain a young-looking disk around an older star. Thus PDS 111 might well be the first high mass equivalent of the "Peter Pan" population among M-dwarfs. Our extensive data set, and in particular our spatially resolved observations of the disk, make PDS 111 the ideal laboratory to study this class of long-lasting disks with dedicated simulations.

*Acknowledgements.* SPHERE was designed and built by a consortium made of IPAG (Grenoble, France), MPIA (Heidelberg, Germany), LAM (Marseille, France), LESIA (Paris, France), Laboratoire Lagrange (Nice, France), INAF-Osservatorio di Padova (Italy), Observatoire de Genève (Switzerland), ETH Zurich (Switzerland), NOVA (Netherlands), ONERA (France) and ASTRON (Netherlands) in collaboration with ESO. SPHERE was funded by ESO, with additional contributions from CNRS (France), MPIA (Germany), INAF (Italy), FINES (Switzerland) and NOVA (Netherlands). Additional funding from EC's 6th and 7th Framework Programmes as part of OPTICON was received (grant number RII3-Ct-2004-001566 for FP6 (2004–2008); 226604 for FP7 (2009–2012); 312430 for FP7 (2013–2016)). We acknowledge the Programme National de Planétologie (PNP) and the Programme National de Physique Stellaire (PNPS) of CNRS-INSU, France, the French Labex OSUG@2020 (Investissements d'avenir – ANR10 LABX56) and LIO (Lyon Institute of Origins, ANR-10-LABX-0066 within the programme Investissements d'Avenir, ANR-11-IDEX-0007), and the Agence Nationale de la Recherche (ANR-14-CE33-0018) for support. A.Z. acknowledges support from ANID – Millennium Science Initiative Program – Center Code NCN2021\_080. This paper makes use of the following ALMA data: ADS/JAO.ALMA#2021.1.01705.S. ALMA is a partnership of ESO (representing its member states), NSF (USA) and NINS (Japan), together with NRC (Canada), MOST and ASIAA (Taiwan), and KASI (Republic of Korea), in cooperation with the Republic of Chile. The Joint ALMA Observatory is operated by ESO, AUI/NRAO and NAOJ. Based on observations obtained with the HERMES spectrograph, which is supported by the Research Foundation - Flanders (FWO), Belgium, the Research Council of KU Leuven, Belgium, the Fonds National de la Recherche Scientifique (F.R.S.-FNRS), Belgium, the Royal Observatory of Belgium, the Observatoire de Genève, Switzerland and the Thüringer Landessternwarte Tautenburg, Germany. This paper includes data collected by the TESS mission. Funding for the TESS mission is provided by the NASA's Science Mission Directorate. P.P. acknowledges funding from the UK Research and Innovation (UKRI) under the UK government's Horizon Europe funding guarantee from ERC (grant agreement No 101076489). This project has received funding from the European Research Council (ERC) under the European Union's Horizon Europe research and innovation program (DUST2PLANETS, grant agreement No. 101053020). This project has received funding from the European Research Council (ERC) under the European Union's Horizon 2020 research and innovation programme (PROTOPLANETS, grant agreement No. 101002188). Part of this research was carried out at the Jet Propulsion Laboratory, California Institute of Technology, under a contract with the National Aeronautics and Space Administration (80NM0018D0004).

## References

- Alcalá, J. M., Manara, C. F., Natta, A., et al. 2017, *A&A*, 600, 20  
Andrews, S. M. 2020, *ARA&A*, 58, 483

- Andrews, S. M., Huang, J., Pérez, L. M., et al. 2018, *ApJ*, 869, L41
- Andrews, S. M., Rosenfeld, K. A., Kraus, A. L., & Wilner, D. J. 2013, *ApJ*, 771, 129
- Artymowicz, P. & Lubow, S. H. 1994, *ApJ*, 421, 651
- Ataiee, S., Pinilla, P., Zsom, A., et al. 2013, *A&A*, 553, L3
- Avenhaus, H., Quanz, S. P., Garufi, A., et al. 2018, *ApJ*, 863, 44
- Bae, J., Isella, A., Zhu, Z., et al. 2023, in *Astronomical Society of the Pacific Conference Series*, Vol. 534, *Astronomical Society of the Pacific Conference Series*, ed. S. Inutsuka, Y. Aikawa, T. Muto, K. Tomida, & M. Tamura, 423
- Bailer-Jones, C. A. L., Rybizki, J., Founesneau, M., Demleitner, M., & Andrae, R. 2021, *AJ*, 161, 147
- Barraza-Alfaro, M., Flock, M., Marino, S., & Pérez, S. 2021, *A&A*, 653, A113
- Beckwith, S. V. W., Sargent, A. I., Chini, R. S., & Guesten, R. 1990, *AJ*, 99, 924
- Bell, C. P. M., Mamajek, E. E., & Naylor, T. 2015, *MNRAS*, 454, 593
- Benisty, M., Dominik, C., Follette, K., et al. 2023, in *Astronomical Society of the Pacific Conference Series*, Vol. 534, *Protostars and Planets VII*, ed. S. Inutsuka, Y. Aikawa, T. Muto, K. Tomida, & M. Tamura, 605
- Benisty, M., Juhász, A., Facchini, S., et al. 2018, *A&A*, 619, A171
- Beuzit, J. L., Vigan, A., Mouillet, D., et al. 2019, *A&A*, 631, A155
- Biller, B., Lacour, S., Juhász, A., et al. 2012, *ApJ*, 753, L38
- Boone, F. 2013, *Experimental Astronomy*, 36, 77
- Bouvier, J., Sousa, A., Pouilly, K., et al. 2023, *A&A*, 672, A5
- Briggs, D. S. 1995, in *American Astronomical Society Meeting Abstracts*, Vol. 187, *American Astronomical Society Meeting Abstracts*, 112.02
- Busso, G., Cacciari, C., Bellazzini, M., et al. 2022, *Gaia DR3 documentation Chapter 5: Photometric data*
- Cardelli, J. A., Clayton, G. C., & Mathis, J. S. 1989, *ApJ*, 345, 245
- Carpenter, J. M., Bouwman, J., Mamajek, E. E., et al. 2009, *ApJS*, 181, 197
- Cauley, P. W. & Johns-Krull, C. M. 2014, *ApJ*, 797, 112
- Close, L. M., Follette, K. B., Males, J. R., et al. 2014, *ApJ*, 781, L30
- Coleman, G. A. & Haworth, T. J. 2020, *MNRAS*, 496, L111
- Czekala, I., Loomis, R. A., Teague, R., et al. 2021, *ApJS*, 257, 2
- da Silva, L., Torres, C. A. O., de La Reza, R., et al. 2009, *A&A*, 508, 833
- de Boer, J., Langlois, M., van Holstein, R. G., et al. 2020, *A&A*, 633, A63
- de Boer, J., Salter, G., Benisty, M., et al. 2016, *A&A*, 595, A114
- de Jong, J. A., Henrichs, H. F., Kaper, L., et al. 2001, *A&A*, 368, 601
- de Juan Ovelar, M., Min, M., Dominik, C., et al. 2013, *A&A*, 560, A111
- Debes, J. H., Poteet, C. A., Jang-Condell, H., et al. 2017, *ApJ*, 835, 205
- Delage, T. N., Okuzumi, S., Flock, M., Pinilla, P., & Dzyurkevich, N. 2022, *A&A*, 658, A97
- Derkink, A. R., Ramírez-Tannus, M. C., Kaper, L., et al. 2024, *A&A*, 681, A112
- Dohlen, K., Langlois, M., Saisse, M., et al. 2008, in *Society of Photo-Optical Instrumentation Engineers (SPIE) Conference Series*, Vol. 7014, *Ground-based and Airborne Instrumentation for Astronomy II*, ed. I. S. McLean & M. M. Casali, 70143L
- Dominik, C. & Dullemond, C. P. 2008, *A&A*, 491, 663
- Dullemond, C. P., Birnstiel, T., Huang, J., et al. 2018, *ApJ*, 869, L46
- Dullemond, C. P. & Dominik, C. 2004, *A&A*, 421, 1075
- ESA. 1997, *VizieR Online Data Catalog*, I/239
- Facchini, S., Pinilla, P., van Dishoeck, E. F., & de Juan Ovelar, M. 2018, *A&A*, 612, A104
- Fedele, D., van den Ancker, M. E., Henning, T., Jayawardhana, R., & Oliveira, J. M. 2010, *A&A*, 510, A72
- Fitton, S., Tofflemire, B. M., & Kraus, A. L. 2022, *Research Notes of the American Astronomical Society*, 6, 18
- Flock, M., Ruge, J. P., Dzyurkevich, N., et al. 2015, *A&A*, 574, A68
- Flores-Rivera, L., Flock, M., & Nakatani, R. 2020, *A&A*, 644, A50
- Franceschi, R., Birnstiel, T., Henning, T., & Sharma, A. 2023, *A&A*, 671, A125
- Fukagawa, M., Tamura, M., Itoh, Y., et al. 2006, *ApJ*, 636, L153
- Fullerton, A. W., Gies, D. R., & Bolton, C. T. 1996, 103, 475
- Gagné, J., David, T. J., Mamajek, E. E., et al. 2020, *ApJ*, 903, 96
- Gaia Collaboration. 2022, *VizieR Online Data Catalog*, I/355
- Garufi, A., Avenhaus, H., Pérez, S., et al. 2020, *A&A*, 633, A82
- Ginski, C., Benisty, M., van Holstein, R. G., et al. 2018, *A&A*, 616, A79
- Ginski, C., Facchini, S., Huang, J., et al. 2021, *ApJ*, 908, L25
- Ginski, C., Ménard, F., Rab, C., et al. 2020, *A&A*, 642, A119
- Ginski, C., Stolker, T., Pinilla, P., et al. 2016, *A&A*, 595, A112
- Gray, R. 2000, *A digital spectral classification atlas*
- Guilloteau, S., Dutrey, A., Piétu, V., & Boehler, Y. 2011, *A&A*, 529, A105
- Hildebrand, R. H. 1983, *QJRAS*, 24, 267
- Hom, E. F. Y., Marchis, F., Lee, T. K., et al. 2007, *Journal of the Optical Society of America A*, 24, 1580
- Huang, J., Andrews, S. M., Pérez, L. M., et al. 2018, *ApJ*, 869, L43
- Jayasinghe, T., Kochanek, C. S., Stanek, K. Z., et al. 2018, *MNRAS*, 477, 3145
- Jorsater, S. & van Moorsel, G. A. 1995, *AJ*, 110, 2037
- Juhász, A. & Facchini, S. 2017, *MNRAS*, 466, 4053
- Karamanis, M. & Beutler, F. 2020, *arXiv e-prints*, arXiv:2002.06212
- Karamanis, M., Beutler, F., & Peacock, J. A. 2021, *MNRAS*, 508, 3589
- Kataoka, A., Tanaka, H., Okuzumi, S., & Wada, K. 2013, *A&A*, 557, L4
- Kausch, W., Noll, S., Smette, A., et al. 2015, *Astronomy & Astrophysics*, 576, A78
- Keppler, M., Penzlin, A., Benisty, M., et al. 2020, *A&A*, 639, A62
- Kiraga, M. 2012, *Acta Astron.*, 62, 67
- Kounkel, M. & Covey, K. 2019, *AJ*, 158, 122
- Kuffmeier, M., Goicovic, F. G., & Dullemond, C. P. 2020, *A&A*, 633, A3
- Kuhn, J. R., Potter, D., & Parise, B. 2001, *ApJ*, 553, L189
- Kurtovic, N. T., Pinilla, P., Penzlin, A. B. T., et al. 2022, *A&A*, 664, A151
- Kurucz, R. L. 1993, *VizieR Online Data Catalog*, VI/39
- Kwan, J., Edwards, S., & Fischer, W. 2007, *ApJ*, 657, 897
- Lallement, R., Capitanio, L., Ruiz-Dern, L., et al. 2018, *A&A*, 616, A132
- Launhardt, R., Loinard, L., Dzib, S. A., et al. 2022, *ApJ*, 931, 43
- Law, C. J., Teague, R., Öberg, K. I., et al. 2023, *ApJ*, 948, 60
- Lesur, G., Ercolano, B., Flock, M., et al. 2022, *arXiv e-prints*, arXiv:2203.09821
- Lomb, N. R. 1976, *Ap&SS*, 39, 447
- Long, F., Andrews, S. M., Rosotti, G., et al. 2022, *ApJ*, 931, 6
- Long, F., Pinilla, P., Herczeg, G. J., et al. 2018, *ApJ*, 869, 17
- Mamajek, E. E. 2009, in *American Institute of Physics Conference Series*, Vol. 1158, *Exoplanets and Disks: Their Formation and Diversity*, ed. T. Usuda, M. Tamura, & M. Ishii, 3–10
- Manara, C. F., Ansdell, M., Rosotti, G. P., et al. 2023, in *Astronomical Society of the Pacific Conference Series*, Vol. 534, *Protostars and Planets VII*, ed. S. Inutsuka, Y. Aikawa, T. Muto, K. Tomida, & M. Tamura, 539
- Manara, C. F., Beccari, G., Da Rio, N., et al. 2013, *A&A*, 558, A114
- Marois, C., Lafrenière, D., Doyon, R., Macintosh, B., & Nadeau, D. 2006, *ApJ*, 641, 556
- Milli, J., Mouillet, D., Lagrange, A. M., et al. 2012, *A&A*, 545, A111
- Miranda, R., Muñoz, D. J., & Lai, D. 2017, *MNRAS*, 466, 1170
- Modigliani, A., Goldoni, P., Royer, F., et al. 2010, in *Society of Photo-Optical Instrumentation Engineers (SPIE) Conference Series*, Vol. 7737, *Observatory Operations: Strategies, Processes, and Systems III*, 773728
- Monnier, J. D., Harries, T. J., Bae, J., et al. 2019, *ApJ*, 872, 122
- Muñoz, D. J. & Lithwick, Y. 2020, *ApJ*, 905, 106
- Muro-Arena, G. A., Benisty, M., Ginski, C., et al. 2020, *A&A*, 635, A121
- Nisini, B., Antonucci, S., Alcalá, J. M., et al. 2018, *A&A*, 609, A87
- Ogilvie, G. I. 2008, *MNRAS*, 388, 1372
- Padgett, D., Koerner, D., Wahhaj, Z., et al. 2006, in *Astronomical Society of the Pacific Conference Series*, Vol. 357, *The Spitzer Space Telescope: New Views of the Cosmos*, ed. L. Armus & W. T. Reach, 97
- Pascucci, I., Testi, L., Herczeg, G. J., et al. 2016, *ApJ*, 831, 125
- Pecaut, M. J. & Mamajek, E. E. 2013, *The Astrophysical Journal Supplement Series*, 208, 9
- Penzlin, A. B. T., Kley, W., Audiffren, H., & Schäfer, C. M. 2022, *A&A*, 660, A101
- Pinilla, P., Kurtovic, N. T., Benisty, M., et al. 2021, *A&A*, 649, A122
- Pinilla, P., Tazzari, M., Pascucci, I., et al. 2018, *ApJ*, 859, 32
- Pyerin, M. A., Delage, T. N., Kurtovic, N. T., et al. 2021, *A&A*, 656, A150
- Ragusa, E., Alexander, R., Calcino, J., Hirsh, K., & Price, D. J. 2020, *MNRAS*, 499, 3362
- Ramírez-Tannus, M. C., Kaper, L., De Koter, A., et al. 2017, *A&A*, 604
- Raskin, G., van Winkel, H., Hensberge, H., et al. 2011, *A&A*, 526, A69
- Ribas, Á., Merín, B., Bouy, H., & Maud, L. T. 2014, *A&A*, 561, A54
- Ricker, G. R., Winn, J. N., Vanderspek, R., et al. 2015, *Journal of Astronomical Telescopes, Instruments, and Systems*, 1, 014003
- Roddi, C., Roddi, F., Northcott, M. J., Graves, J. E., & Jim, K. 1996, *ApJ*, 463, 326
- Rojas, G., Gregorio-Hetem, J., & Hetem, A. 2008, *MNRAS*, 387, 1335
- Scargle, J. D. 1982, *ApJ*, 263, 835
- Shi, J.-M., Krolik, J. H., Lubow, S. H., & Hawley, J. F. 2012, *ApJ*, 749, 118
- Sicilia-Aguilar, A., Henning, T., Dullemond, C. P., et al. 2011, *ApJ*, 742, 39
- Siess, L., Dufour, E., & Forestini, M. 2000, *A&A*, 358, 593
- Silverberg, S. M., Wisniewski, J. P., Kuchner, M. J., et al. 2020, *ApJ*, 890, 106
- Skrutskie, M. F., Cutri, R. M., Stiening, R., et al. 2006, *AJ*, 131, 1163
- Smette, A., Sana, H., Noll, S., et al. 2015, *A&A*, 576, A77
- Stapper, L. M. & Ginski, C. 2022, *A&A*, 668, A50
- Tazzari, M., Beaujean, F., & Testi, L. 2018, *MNRAS*, 476, 4527
- Tazzari, M., Testi, L., Ercolano, B., et al. 2016, *A&A*, 588, A53
- Teague, R. 2019, *The Journal of Open Source Software*, 4, 1220
- Torres, C. A. O., Quast, G., de La Reza, R., Gregorio-Hetem, J., & Lepine, J. R. D. 1995, *AJ*, 109, 2146
- Torres, C. A. O., Quast, G. R., Melo, C. H. F., & Sterzik, M. F. 2008, in *Handbook of Star Forming Regions*, Volume II, ed. B. Reipurth, Vol. 5, 757
- Trapman, L., Ansdell, M., Hogerheijde, M. R., et al. 2020, *A&A*, 638, A38
- Trapman, L., Facchini, S., Hogerheijde, M. R., van Dishoeck, E. F., & Bruderer, S. 2019, *A&A*, 629, A79
- Valegård, P. G., Ginski, C., Dominik, C., et al. 2022, *A&A*, 668, A25
- Valegård, P. G., Waters, L. B. F. M., & Dominik, C. 2021, *A&A*, 652, A133
- van Holstein, R. G., Girard, J. H., de Boer, J., et al. 2020, *A&A*, 633, A64

- van Holstein, R. G., Snik, F., Girard, J. H., et al. 2017, in Society of Photo-Optical Instrumentation Engineers (SPIE) Conference Series, Vol. 10400, Society of Photo-Optical Instrumentation Engineers (SPIE) Conference Series, ed. S. Shaklan, 1040015
- Vernet, J., Dekker, H., D’Odorico, S., et al. 2011, A&A, 536, A105
- Villenave, M., Benisty, M., Dent, W. R. F., et al. 2019, A&A, 624, A7
- Wagner, K., Leisenring, J., Cugno, G., et al. 2024, AJ, 167, 181
- Wahhaj, Z., Cieza, L., Koerner, D. W., et al. 2010, ApJ, 724, 835
- Woitke, P., Min, M., Pinte, C., et al. 2016, A&A, 586, A103
- Wolf, C., Onken, C. A., Luvaul, L. C., et al. 2018, PASA, 35, e010
- Wright, E. L., Eisenhardt, P. R. M., Mainzer, A. K., et al. 2010, AJ, 140, 1868
- Zacharias, N., Finch, C., Girard, T., et al. 2009, VizieR Online Data Catalog, I/315
- Zhang, S., Zhu, Z., Huang, J., et al. 2018, ApJ, 869, L47
- Zhu, Z., Nelson, R. P., Hartmann, L., Espaillat, C., & Calvet, N. 2011, ApJ, 729, 47
- Zhu, Z., Zhang, S., Jiang, Y.-F., et al. 2019, ApJ, 877, L18

- 
- <sup>1</sup> Anton Pannekoek Institute for Astronomy (API), University of Amsterdam, Science Park 904, 1098 XH Amsterdam, The Netherlands, e-mail: a.r.derinkink@uva.nl
- <sup>2</sup> School of Natural Sciences, University of Galway, University Road, H91 TK33 Galway, Ireland
- <sup>3</sup> Mullard Space Science Laboratory, University College London, Holmbury St Mary, Dorking, Surrey RH5 6NT, UK
- <sup>4</sup> Max-Planck-Institut für extraterrestrische Physik, Giessenbachstrasse 1, 85748 Garching, Germany
- <sup>5</sup> Instituut voor Sterrenkunde, KU Leuven, Celestijnenlaan 200D bus 2401, 3001 Leuven, Belgium
- <sup>6</sup> Jet Propulsion Laboratory, California Institute of Technology, Pasadena, CA, USA
- <sup>7</sup> Department of Physics and Astronomy, University of Rochester, Rochester, NY, USA
- <sup>8</sup> Université Côte d’Azur, Observatoire de la Côte d’Azur, CNRS, Laboratoire Lagrange, Bd de l’Observatoire, CS 34229, 06304 Nice cedex 4, France
- <sup>9</sup> Université Grenoble Alpes, CNRS, Institut de Planétologie et d’Astrophysique (IPAG), F-38000 Grenoble, France
- <sup>10</sup> University Observatory, Faculty of Physics, Ludwig-Maximilians-Universität, Scheinerstr. 1, D-81679 Munich, Germany
- <sup>11</sup> Department of Physics and Astronomy “Galileo Galilei” (DFA), University of Padua, via Marzolo 8, 35131 Padua, Italy
- <sup>12</sup> INAF, Osservatorio Astrofisico di Arcetri, Largo Enrico Fermi 5, I-50125 Firenze, Italy
- <sup>13</sup> Leiden Observatory, Leiden University, 2300 RA Leiden, The Netherlands
- <sup>14</sup> European Southern Observatory, Alonso de Córdova 3107, Casilla 19001, Vitacura, Santiago, Chile
- <sup>15</sup> Department of Astronomy, University of Michigan, 323 West Hall, 1085 S. University Avenue, Ann Arbor, MI 48109, USA
- <sup>16</sup> Max Planck Institute for Astronomy, Königstuhl 17, 69117, Heidelberg, Germany
- <sup>17</sup> Institute of Astronomy, University of Cambridge, Madingley Road, Cambridge CB3 0HA, UK
- <sup>18</sup> Institute for Astronomy, University of Hawai’i at Manoa, Honolulu, HI 96822, USA
- <sup>19</sup> Instituto de Estudios Astrofísicos, Facultad de Ingeniería y Ciencias, Universidad Diego Portales, Av. Ejército Libertador 441, Santiago, Chile
- <sup>20</sup> Millennium Nucleus on Young Exoplanets and their Moons (YEMS), Chile



### Appendix A: Flux calibrated stacked total intensity and polarimetric images

In Fig. A.2 we show the de-rotated and stacked total intensity image, which contains the disk and stellar signal. In Fig. A.1 we show the flux calibrated Stokes  $Q$ ,  $U$ ,  $Q_\phi$ ,  $U_\phi$  images. Flux calibration was done with the central star as the reference source. For this purpose we used the flux calibration frames which were taken before and after the science images and in which the star is removed from the coronagraph and a neutral density filter inserted to prevent saturation. We measured the central star flux using aperture photometry. We then translate detector counts into units of surface brightness via the known H-band magnitude of the primary star.

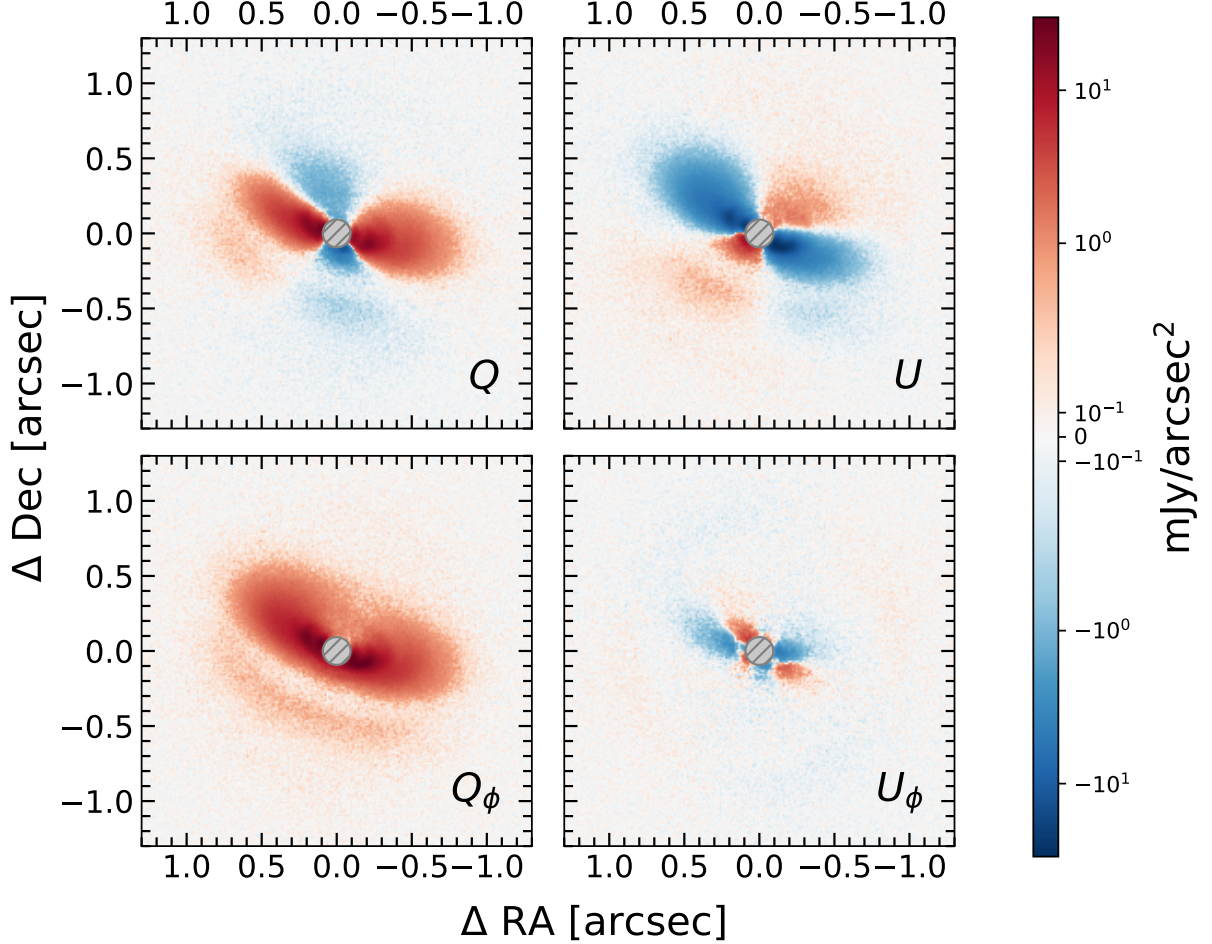


**Fig. A.1.** Flux calibrated polarimetric images. The directly measured Stokes  $Q$  and  $U$  parameters are shown in the top row and the derived azimuthal Stokes  $Q_\phi$  and  $U_\phi$  parameters in the bottom row. All images are shown on the same (logarithmic) scale, symmetric around 0. In all images, the gray, hashed circle in the center marks the area that was covered by a coronagraphic mask.

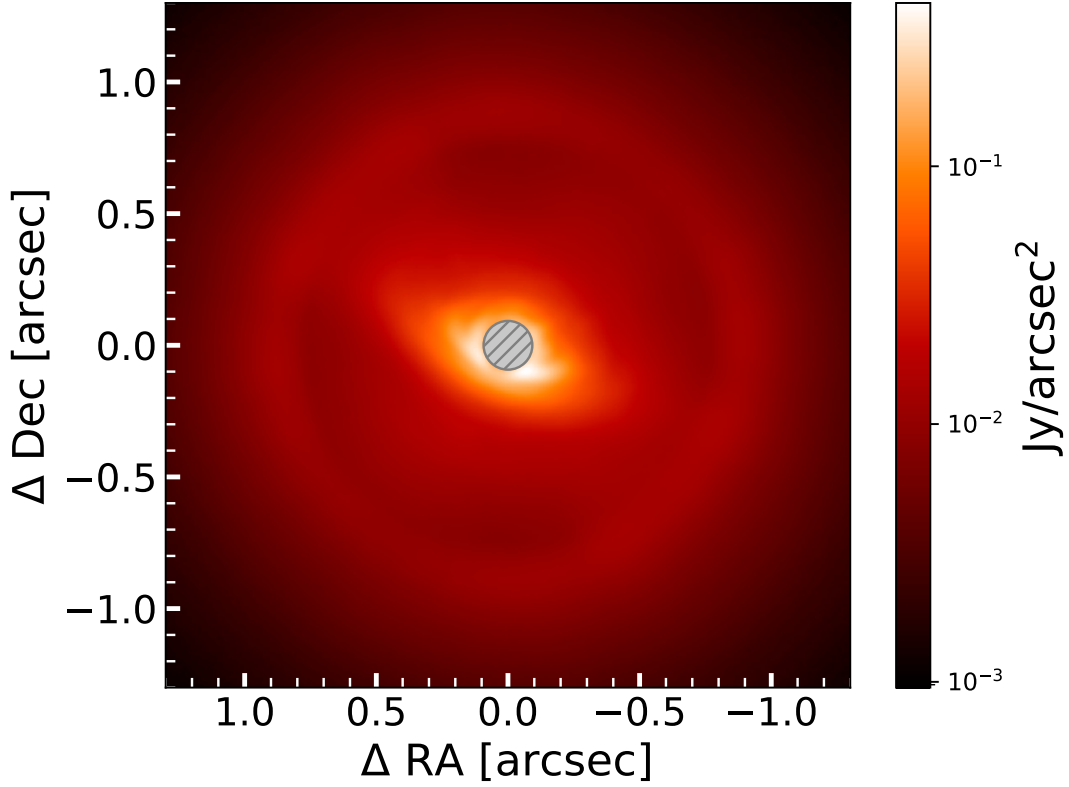


**Fig. A.2.** Flux calibrated stacked total intensity image. We note that in this image the stellar light was not removed. The bright ring visible on the outer edge of the image shows the adaptive optics correction radius which shows bright stellar speckle signal (smoothed out by the field rotation during observations). The signal of the disk is faintly visible close to the coronagraph. The image is shown on a (logarithmic) scale, symmetric around 0. The grey, hashed circle in the center marks the area that was covered by a coronagraphic mask.

## Appendix B: Stellar atmosphere model fit

The  $\chi^2$  values from atmospheric model fitting are shown in Fig. B.1 and a subset of the models, including the best fit, is shown in Fig. 2. The fitting range is from 402 nm to 430 nm based on Gray (2000).

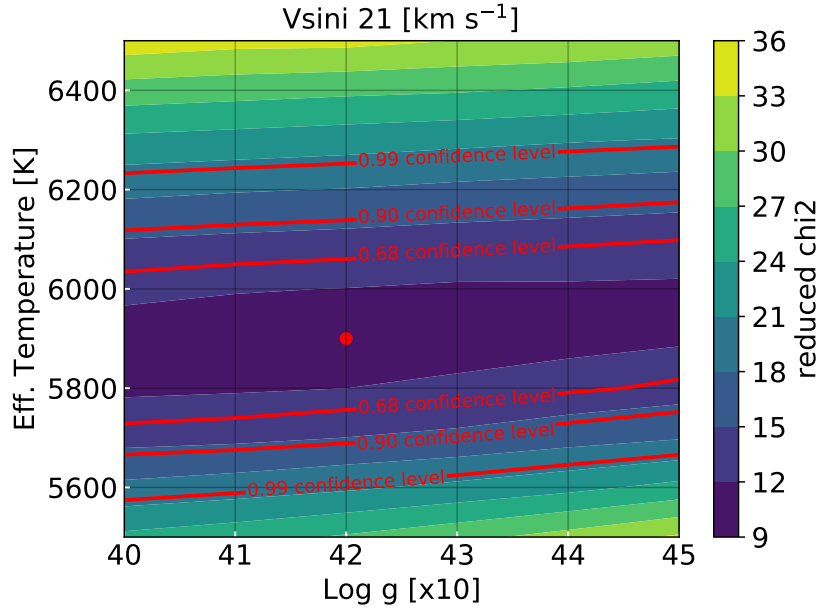


**Fig. B.1.** Resulting reduced  $\chi^2$  values from atmospheric model fitting. The Kurucz models have different temperatures and surface gravities and a constant  $v \sin i$ . The lowest  $\chi^2$  value is indicated with a red dot.

### Appendix C: SED

In this section we show the B- and V-band from Gaia photometry and the SED discussed in Sec. 4.1. Figs. C.1 and C.2 shows the B- and V-band measurements converted from Gaia measurements (Gaia Collaboration 2022; Jayasinghe et al. 2018). Fig. C.3 shows the SED and Table C.1.

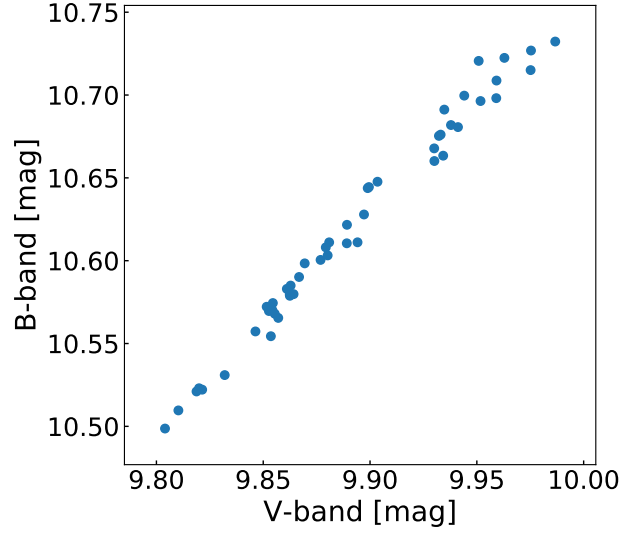


**Fig. C.1.** B- and V-band photometry converted from Gaia measurements. The B- and V-band measurements show variations.

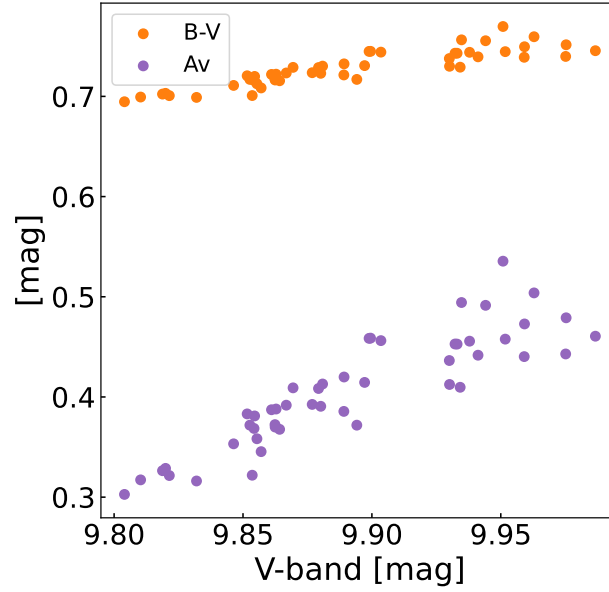


**Fig. C.2.**  $B-V$  color and  $A_V$  shown for V-band measurements determined from Gaia.  $B-V$  shows a slight increase with increasing V-band magnitude. The reported  $A_V$  follows from  $A_V = R_V * E(B-V)$  where  $E(B-V)$  is determined by comparing the observed  $B-V$  to the intrinsic  $(B-V)_0$  of 0.597 mag (interpolated from table 6 in Pecaut & Mamajek (2013) for a star of 5900 K) and also increases with an increasing V-band measurement. The  $A_V$  values are slightly higher than determined by the SED fit.

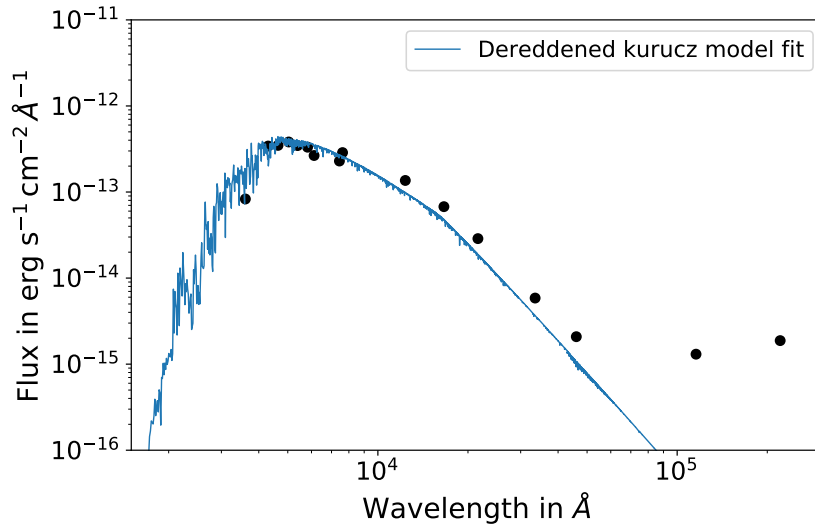


**Fig. C.3.** The SED following from Kurucz model fitting to optical photometry, discussed in Sec. 4.1. The model and photometry are dereddened using Cardelli’s extinction law. Infrared excess is observed from the J-band on toward redder wavelengths.

**Table C.1.** Photometry used for SED fitting.

| Band                         | Flux [mag] | error [mag] | effective wavelength [Å] | reference                                 |
|------------------------------|------------|-------------|--------------------------|---|
| <i>u</i> (SDSS)              | 11.638     | 0.028       | 3608                     | <a href="#">Wolf et al. (2018)</a>        |
| <i>B</i> (Johnson)           | 10.70      | 0.038       | 4299                     | See Sec. 3.1                              |
| <i>g</i> (SDSS)              | 10.506     | 0.12        | 4639                     | <a href="#">Wolf et al. (2018)</a>        |
| <i>G<sub>BP</sub></i> (Gaia) | 10.0731    | 0.00766     | 5036                     | <a href="#">Gaia Collaboration (2022)</a> |
| <i>V</i> (Johnson)           | 9.97       | 0.22        | 5394                     | See Sec. 3.1                              |
| <i>G</i> Gaia                | 9.69303    | 0.00341     | 5822                     | <a href="#">Gaia Collaboration (2022)</a> |
| <i>r</i> (SDSS)              | 9.943      | 0.04        | 6122                     | <a href="#">Wolf et al. (2018)</a>        |
| <i>i</i> (SDSS)              | 9.465      | 0.05        | 7439                     | <a href="#">Wolf et al. (2018)</a>        |
| <i>G<sub>RP</sub></i> (Gaia) | 9.11425    | 0.00612     | 7620                     | <a href="#">Gaia Collaboration (2022)</a> |
| <i>J</i> (2MASS)             | 8.403      | 0.02        | 12350                    | <a href="#">Skrutskie et al. (2006)</a>   |
| <i>H</i> (2MASS)             | 8.058      | 0.55        | 16620                    | <a href="#">Skrutskie et al. (2006)</a>   |
| <i>K<sub>s</sub></i> (2MASS) | 7.932      | 0.024       | 21590                    | <a href="#">Skrutskie et al. (2006)</a>   |
| <i>W1</i> (WISE)             | 7.862      | 0.024       | 33526                    | <a href="#">Wright et al. (2010)</a>      |
| <i>W2</i> (WISE)             | 7.662      | 0.02        | 46028                    | <a href="#">Wright et al. (2010)</a>      |
| <i>W3</i> (WISE)             | 4.246      | 0.014       | 115608                   | <a href="#">Wright et al. (2010)</a>      |
| <i>W4</i> (WISE)             | 1.083      | 0.01        | 220883                   | <a href="#">Wright et al. (2010)</a>      |

## Appendix D: EW measurements

The EW measurements of several lines are reported in Tab. D.1.

**Table D.1.** EW measurements in Å after stellar model subtraction.

|            | $\lambda_{rest}$ (in nm) | 28-11-2021 | 07-12-2021 | 20-10-2022 | 28-10-2022 |
|------------|--------------------------|------------|------------|------------|------------|
| H $\alpha$ | 656.279                  | -1.274     | -1.873     | -1.567     | -0.811     |
| H $\beta$  | 486.135                  | -0.240     | 0.198      | -0.071     | -0.239     |
| Li I       | 670.78                   | 0.237      | 0.239      | 0.249      | 0.253      |
| Ca II-i    | 849.802                  | 0.099      | 0.078      | 0.052      | 0.031      |
| Ca II-ii   | 854.209                  | 0.411      | 0.406      | 0.249      | 0.311      |
| Ca II-iii  | 866.214                  | 0.142      | 0.155      | 0.111      | 0.167      |
| He I       | 1083.33                  | 0.669      | 1.813      |            |            |

## Appendix E: Ellipse fitting

Fig. E.1 and E.2 highlight the disk structures and the overlaid ellipses.

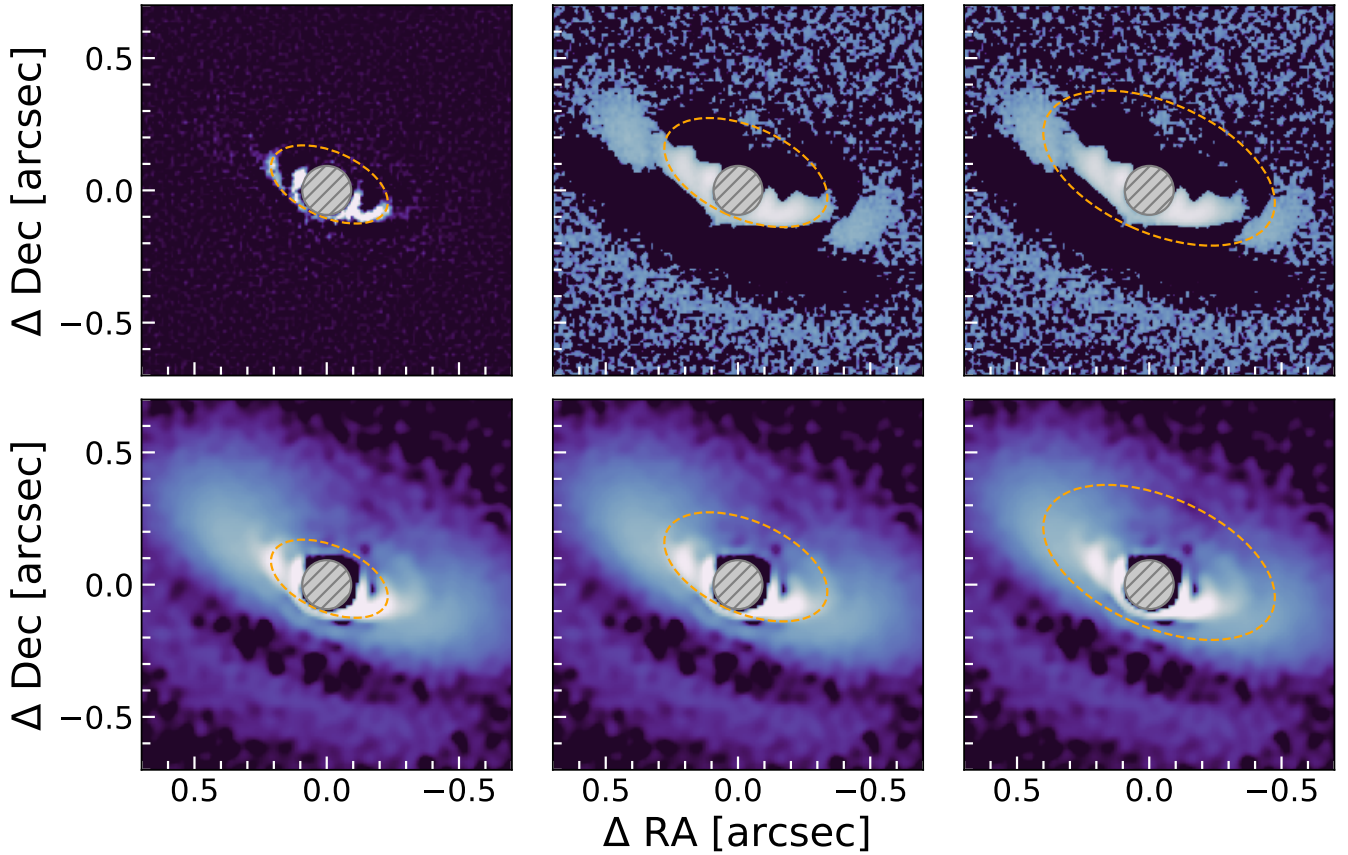


**Fig. E.1.** SPHERE scattered light data after high pass filtering (top row) and deconvolution (bottom row). The color map was adjusted in each panel to highlight the most prominent sub-structure in the disk. We overplot ellipses tracing the two inner rings and the following gap from left to right.

## Appendix F: Components of the visibility fitting

Fig. F.1 shows a sketch of the components of the intensity profile that are assumed for the visibility fitting of the dust continuum emission of the disk around PDS 111 observed with ALMA.

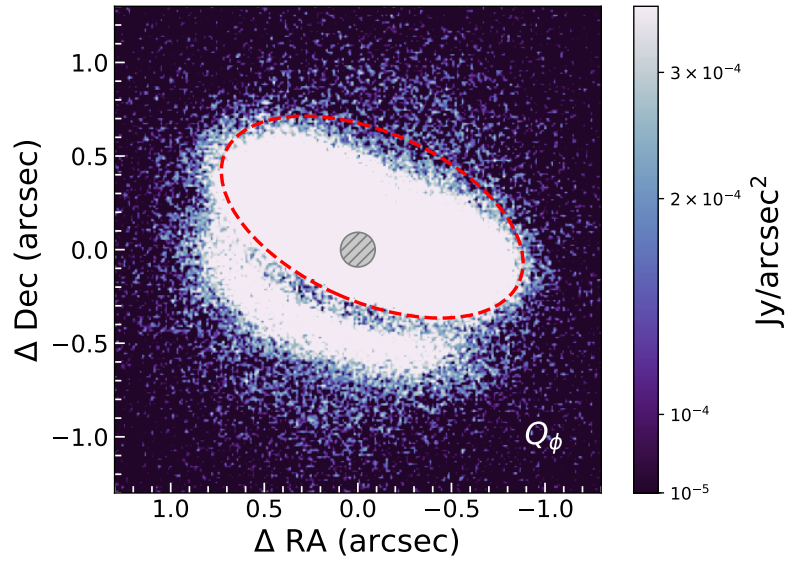


**Fig. E.2.** SPHERE  $Q_\phi$  image shown on a saturated color map to highlight the outer edge of the disk. The red dashed line marks the ellipse also shown in Fig. 7, which traces the outer edge. Note that due to the scattering phase function the disk far side is faint, and thus appears only at low S/N.

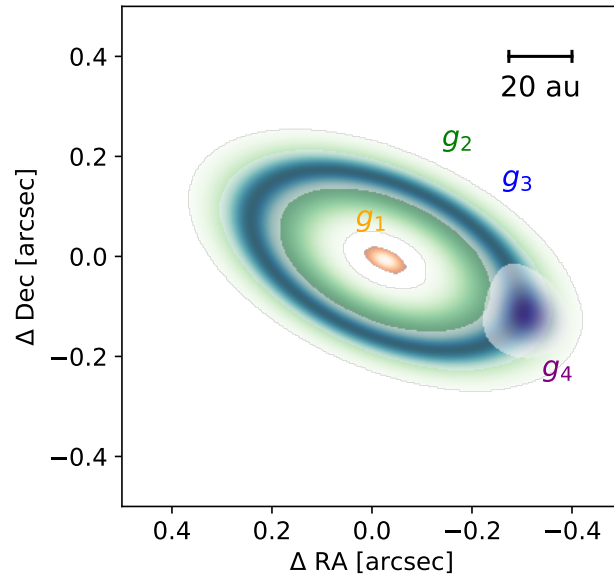


**Fig. F.1.** Schematic of PDS 111 components of the model used to fit the visibilities from the ALMA observations. The model components do not reflect the relative flux of contribution.

## Appendix G: Channel map of the $^{12}\text{CO}$

Fig. G.1 shows the channel maps of  $^{12}\text{CO}$  of PDS 111 from ALMA observations

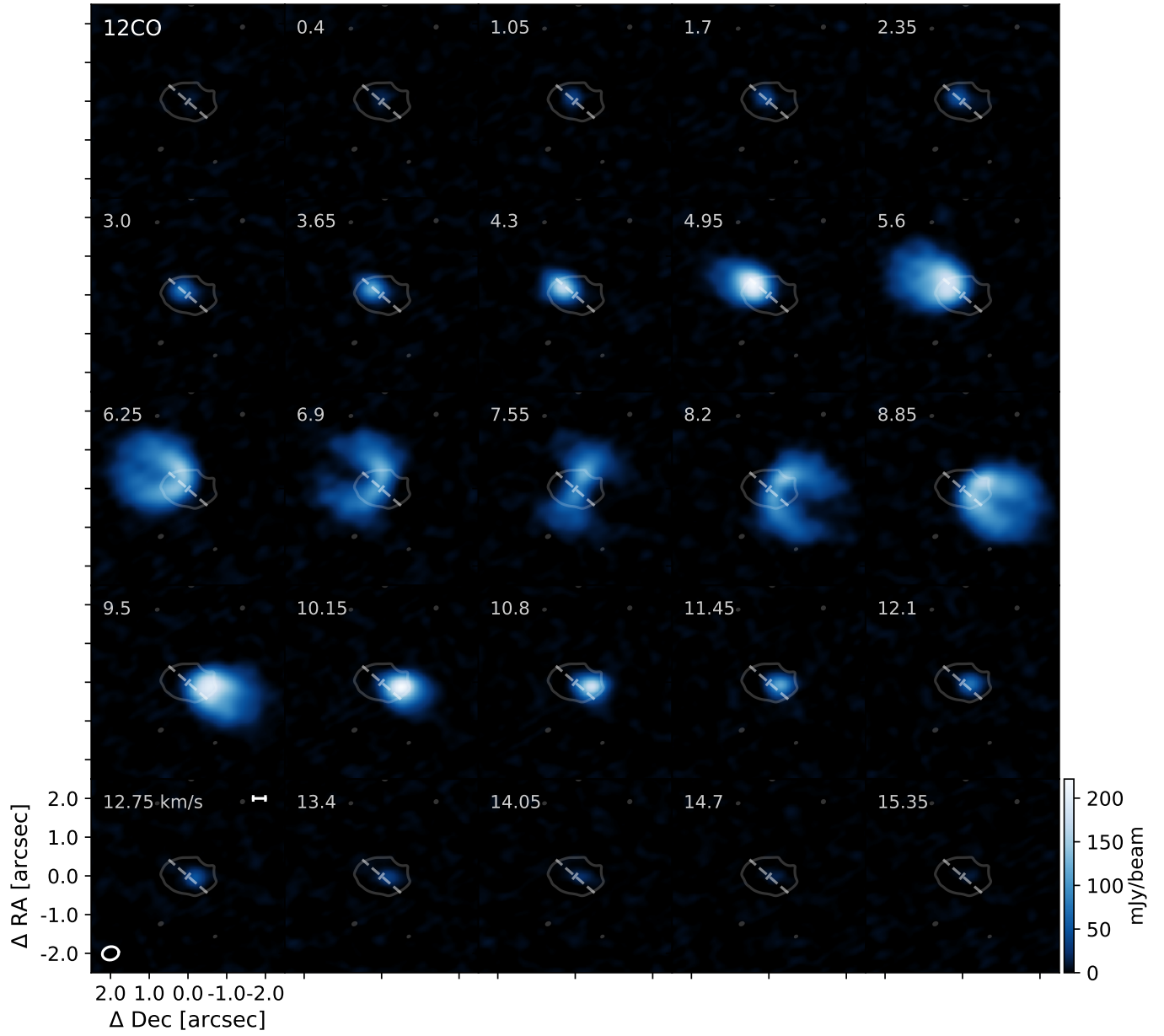


**Fig. G.1.** Channel maps of  $^{12}\text{CO}$  of PDS 111. The gray contours are at the  $5 \times \sigma$  level of the continuum emission. The scale bar in the left panel represents a scale of 50 au. The dashed line is the PA of the continuum emission in the disk.